

Article

Fe₃O₄ Nanoparticle-Decorated Bimodal Porous Carbon Nanocomposite Anode for High-Performance Lithium-Ion Batteries

Juti Rani Deka¹, Diganta Saikia², Yuan-Hung Lai², Hsien-Ming Kao^{2,*}  and Yung-Chin Yang^{1,*}

¹ Institute of Materials Science and Engineering, National Taipei University of Technology, Taipei 106344, Taiwan; juti.deka@gmail.com

² Department of Chemistry, National Central University, Zhongli 320317, Taiwan; digantas@gmail.com (D.S.); s12304777@gmail.com (Y.-H.L.)

* Correspondence: hmkao@cc.ncu.edu.tw (H.-M.K.); ycyang@ntut.edu.tw (Y.-C.Y.); Tel.: +886-3-4275054 (H.-M.K.); +886-2-27712171 (ext. 2762) (Y.-C.Y.); Fax: +886-3-4227664 (H.-M.K.); +886-2-27317185 (Y.-C.Y.)

Abstract: A new nanocomposite system based on Fe₃O₄ nanoparticles confined in three-dimensional (3D) dual-mode cubic porous carbon is developed using the nanocasting and wet-impregnation methods to assess its performance as an anode for lithium-ion batteries. Several Fe₃O₄ precursor concentrations are chosen to optimize and determine the best-performing nanocomposite composition. The cubic mesoporous carbon CMK-9 offers a better ability for the Fe₃O₄ nanoparticles to be accommodated inside the mesopores, efficiently buffering the variation in volume and equally enhancing electrode/electrolyte contact for rapid charge and mass transfer. Among the prepared nanocomposites, the Fe₃O₄(13)@C9 anode delivers an excellent reversible discharge capacity of 1222 mA h g⁻¹ after 150 cycles at a current rate of 100 mA g⁻¹, with a capacity retention of 96.8% compared to the fourth cycle (1262 mA h g⁻¹). At a higher current rate of 1000 mA g⁻¹, the nanocomposite anode offers a superior discharge capacity of 636 mA h g⁻¹ beyond 300 cycles. The present study reveals the use of a 3D mesoporous carbon material as a scaffold for anchoring Fe₃O₄ nanoparticles with impressive potential as an anode for new-generation lithium-ion batteries.

Keywords: mesoporous carbon; Fe₃O₄; nanocomposite; anode; lithium-ion battery



Citation: Deka, J.R.; Saikia, D.; Lai, Y.-H.; Kao, H.-M.; Yang, Y.-C. Fe₃O₄ Nanoparticle-Decorated Bimodal Porous Carbon Nanocomposite Anode for High-Performance Lithium-Ion Batteries. *Batteries* **2023**, *9*, 482. <https://doi.org/10.3390/batteries9100482>

Academic Editor: Dino Tonti

Received: 15 August 2023

Revised: 8 September 2023

Accepted: 12 September 2023

Published: 22 September 2023



Copyright: © 2023 by the authors. Licensee MDPI, Basel, Switzerland. This article is an open access article distributed under the terms and conditions of the Creative Commons Attribution (CC BY) license (<https://creativecommons.org/licenses/by/4.0/>).

1. Introduction

Lithium-ion batteries (LIBs) are one of the most proven technologies for supporting a reduction in fossil fuel dependency and attaining environmental sustainability. The ever-increasing demand for LIBs is a result of their utilization in a range of applications, from compact electronic devices to electric vehicles (EVs) and the electricity grid [1,2]. However, high energy and power density are essential for next-generation LIBs to satisfy the growing needs of future high-end devices. As mass-produced graphite anodes have a lower theoretical capacity of 372 mA h g⁻¹, LIBs with these anodes are not suitable for high-power-consumption devices. Therefore, exploring anode materials with high capacity and rate capabilities, extended cycle life and cost-effectiveness is a prime requisite for the development of a viable high-energy-density, high-power battery. In this connection, transition metal oxide (TMO)-based anodes and polymetallic oxides with yolk-shell structures have been greatly explored for LIBs because of their higher specific capacities [3–12]. Among them, Fe₃O₄ is specifically notable, owing to its high theoretical capacity (~924 mA h g⁻¹), as well as its abundance, lower cost and environmental friendliness [13,14]. However, its use as an anode in LIBs is limited owing to its lower electronic conductivity and its large volume variation while charging/discharging, resulting in inferior rate capability and poor cycling. Studies on nanocomposite materials have shown that carbon materials are favorable to the electrode materials of TMOs, as they enhance their electrical conductivity

and reduce the volume variation at the time of charging/discharging [15,16]. Therefore, to improve their electrochemical performance, various carbon forms, including carbon nanotubes (CNTs) [17], carbon nanofibers (CNFs) [18], graphene [19], reduced graphene oxide (rGO) [20], porous carbons [21], carbon hollow spheres [22] and carbon coating [21,23], have been introduced, using Fe_3O_4 nanostructures to make composite anodes. For instance, Dillon and coworkers prepared a nanostructured Fe_3O_4 /SWNT anode that delivered a capacity of $\sim 680 \text{ mA h g}^{-1}$ after 100 cycles at a current rate of 5C [17]. The CNFs- Fe_3O_4 anode developed by Calderón and coworkers provided a discharge capacity of 699 mA h g^{-1} after 60 cycles at a current rate of 100 mA g^{-1} [18]. Zhao's group synthesized a 3D hierarchical sandwich-structured Fe_3O_4 @C/graphene nanocomposite anode that provided a capacity of $901.5 \text{ mA h g}^{-1}$ after 200 cycles at a current rate of 200 mA g^{-1} [19]. Zhang and coworkers fabricated Fe_3O_4 @rGO composite and achieved a capacity of 1296 mA h g^{-1} after 100 cycles at 100 mA g^{-1} [20]. Sun's group prepared an Fe_3O_4 @PNC anode, which delivered a reversible capacity of 988 mA h g^{-1} at a current density of 200 mA g^{-1} after 100 cycles [23]. Another promising kind of material that exhibits considerable appeal in the design of composites with Fe_3O_4 nanoparticles (NPs) is ordered mesoporous carbons (OMCs) [24,25]. OMCs can be synthesized through either the direct self-assembly [26,27] or nanocasting (hard-template) [28,29] routes. These OMCs have several notable properties, namely, high surface area, highly ordered mesopores, uniform pore size distribution and considerable pore volume. The OMCs produced by the nanocasting approach are highly crystalline and are mostly immune to reaction conditions. The nanocasting process generates material with a nearly identical negative replica of the template it used for the synthesis. Therefore, some pore structures are feasible with the nanocasting process only depending on the morphology of the templates chosen (e.g., ordered mesoporous silicas, colloidal silicas, zeolites, alumina membranes, etc.) [30]. Various ordered mesoporous carbons (2D/3D, rod type/tube type, hexagonal/cubic, etc.), OMCs with additional framework components and different monolithic carbons can be synthesized using specific templates following the nanocasting procedure. Conversely, the self-assembly method provides lower-carbon-yield OMCs with a comparatively poor degree of crystallinity. In addition, reaction ambience affects the development of the mesostructure in this self-assembly approach. While the mesoporous silica SBA-15 template generates 2D hexagonal OMCs, such as CMK-3 and CMK-5, the KIT-6 template produces three-dimensional cubic OMCs, namely CMK-8 and CMK-9. Sucrose carbonization in SBA-15 and KIT-6 produces CMK-3 and CMK-8, respectively, with rod-type formations. When furfuryl alcohol is carbonized inside SBA-15 or KIT-6, it creates the tubular OMCs CMK-5 and CMK-9, respectively. Both CMK-5 and CMK-9 possess dual-mode porosity, with one type of pore being generated between the adjacent nanotubes and another type of pore being obtained from inside the tube. While CMK-5 possesses hexagonal arrangements of nanotube networks, CMK-9 exhibits cubic bicontinuous arrays of nanotube networks [31,32]. Among the CMK series of OMCs with diverse pore structures, only CMK-3 and CMK-5 OMCs have been used to fabricate composites with Fe_3O_4 [33,34]. However, the CMK-9 type of OMC has not been fully exploited for composite anodes, especially with Fe_3O_4 . Therefore, CMK-9 OMC has potential as a support material in the design of new nanocomposite anodes and the study of their performance in LIBs.

In this study, ordered mesoporous carbon CMK-9 is encapsulated with Fe_3O_4 nanoparticles (NPs) for the first time to design a nanocomposite anode for LIBs. CMK-9, an OMC, has the ability to confine the Fe_3O_4 NPs inside the mesopores and, therefore, can prohibit the agglomeration of the nanoparticles and buffer volume variation during the charging and discharging process. Moreover, the interconnected mesopores of CMK-9 facilitate the infiltration of electrolyte into the nanopores, improves mass and charge transfer and thereby boosts electrochemical performances. The higher surface area of CMK-9 can also increase the active sites for Li-ion storage. The 3D dual-mode mesoporous framework of Fe_3O_4 @C9 (CMK-9 denoted as C9) nanocomposite is synthesized by a combination of nanocasting and wet-impregnation process. A series of nanocomposites was prepared by varying the

amount of Fe_3O_4 precursor. The structural, textural, morphological and chemical states of $\text{Fe}_3\text{O}_4@\text{C9}$ nanocomposite are analyzed by XRD, Raman spectroscopy, N_2 -sorption isotherms, TEM and XPS measurements. The newly developed Fe_3O_4 nanoparticle encapsulated CMK-9 nanocomposite as an anode facilitates better electronic conductivity and lithium-ion diffusion. As a result, electrochemical performances, namely higher capacity, superior rate capability and cycle life, improve substantially. The present work brings forth a better objective on customization of the nanocomposite anode by 3D dual-mode mesoporous carbon and metal oxide nanoparticles for high capability LIBs.

2. Experimental Section

2.1. Preparation of $\text{Fe}_3\text{O}_4@\text{C9}$ Nanocomposite

The CMK-9 was prepared by using mesoporous silica KIT-6 as the template, following the procedures mentioned elsewhere [16]. A total of 0.3 g of CMK-9 was mixed with 30 mL 1 M HNO_3 acid and stirred for 24 h at 25 °C to functionalize the surface of CMK-9. The mixture was further sonicated for 2 h at 60 °C. The resulting product was then filtered, washed and dried at 70 °C for 24 h to obtain HNO_3 -acid-treated surface-functionalized CMK-9. The acid treatment presents oxygen comprising surface groups such as carboxyl, hydroxyl, carbonyl, etc., on the surface of CMK-9. At the time of incorporation of metal oxide precursor into the CMK-9, these negatively charged surface groups interact with positively charged metal ions and assist in adsorbing most of the metal ions inside the mesopores of CMK-9. Further heat treatment converts these metal ions into metal oxide nanoparticles embedded finely in the mesopores of CMK-9.

To develop Fe_3O_4 NPs encapsulated CMK-9, named $\text{Fe}_3\text{O}_4@\text{C9}$, five different amounts of $\text{Fe}(\text{NO}_3)_3 \cdot 9\text{H}_2\text{O}$ (0.049, 0.109, 0.187, 0.291, 0.436 g) were combined with ethyl alcohol (20 mL) and subsequently 0.25 g of nitric-acid-treated CMK-9 was added to the solution. Afterwards, the mixture was ultrasonically agitated for 2 h and then placed under a fume hood at 50 °C with slow stirring to evaporate the solvent. The material was further dried in an oven at 70 °C for 1 h and then transferred to a tube furnace and calcined at 550 °C for 4 h in nitrogen ambience at a heating rate of 1 °C min^{-1} . After cooling down to ambient temperature, the final black solid product of $\text{Fe}_3\text{O}_4@\text{C9}$ was obtained. Based on the theoretical calculation of Fe_3O_4 (wt.%) impregnation, the sample was denoted as $\text{Fe}_3\text{O}_4(x)@\text{C9}$, where $x = 4, 8, 13, 18$ and 25 for 0.049, 0.109, 0.187, 0.291 and 0.436 g of precursor, respectively.

To prepare pristine Fe_3O_4 NPs, 20 mmol of $\text{Fe}(\text{NO}_3)_3 \cdot 9\text{H}_2\text{O}$ and 5 mmol of urea (i.e., $(\text{NH}_2)_2\text{CO}$) were dissolved in 40 mL DI H_2O under stirring. The resulting solution was then poured into a 50 mL autoclave and processed hydrothermally at 180 °C for 5 h. The material thus obtained was filtered, washed with DI water and ethyl alcohol, and subsequently dried overnight at 70 °C. The resultant material was calcined at 600 °C for 4 h in N_2 ambience with 1 °C min^{-1} rate of heating to obtain the pristine Fe_3O_4 NPs.

2.2. Fabrication of LIBs

The anode was fabricated by combining active material, Super P carbon (Sigma-Aldrich, St. Louis, MO, USA) and PVdF (Sigma-Aldrich) in the weight ratios of 70:20:10 in *n*-methyl-2-pyrrolidone (Sigma-Aldrich). The mixture was stirred at 300 rpm for more than 4 h, and the resultant black slurry was used to coat Cu foil. The coated Cu foil was dried later in an oven at 70 °C for 12 h, and circular pieces of diameter 10 mm were made. The mass loading of the active material was nearly 1.4 mg cm^{-2} . For assembling the LIBs inside the glove box, CR2032 coin cell was used along with Li metal foil. Then, 1 M LiPF_6 in EC/DEC (1:1, *v/v*) was used as electrolyte, while polypropylene (PP) membrane was chosen for separator. The average pore size of the PP membrane was around 43 nm with porosity of 41%.

2.3. Characterization Methods

Wiggler-A X-ray beamline from the National Synchrotron Radiation Research Center in Taiwan was utilized to measure the small-angle XRD patterns. Shimadzu LabX XRD-6000 diffractometer was employed for the analysis of wide-angle XRD patterns. Specific surface area, pore volume and pore size of the nanocomposites were estimated by measuring the nitrogen adsorption/desorption isotherms at 77 K using a Quantachrome autosorb iQ-2 instrument. Thermogravimetric analysis (TGA) was executed in a TA Instruments Q50 analyzer to evaluate the thermal behavior of the nanocomposites in air ambience at a heating rate of $10\text{ }^{\circ}\text{C min}^{-1}$. Raman spectroscopic measurements of the nanocomposites were conducted in a UniRaman spectrometer supplied by Protrustech Co., Ltd. (Tainan City, Taiwan) X-ray photoelectron spectroscopy (XPS) was accomplished by using a Thermo VG Scientific Sigma Probe spectrometer that included Al K_{α} X-ray source with beam size of $400\text{ }\mu\text{m}$. The microstructures of the nanocomposites were investigated in a JEOL JEM-2100 HRTEM. Hitachi S-800 FESEM was used for the monitoring of the morphology of the nanocomposite.

For electrochemical characterization, Autolab PGSTAT302 instrument was employed to measure the cyclic voltammetry (CV) of the nanocomposite electrodes. LANHE CT2001A battery testing instrument was utilized to analyze the galvanostatic charge–discharge cycles in the voltage region of 0.01–3 V. Autolab PGSTAT302 instrument was applied to measure the electrochemical impedance spectroscopy (EIS) in the frequency limits of 10^5 to 10^{-2} Hz. For the analysis of the material after cycles, the electrode was recovered from the cycled cell by disassembling it and then cleaned with EC and dried. The morphological and microstructural modifications of the cycled electrode were assessed by SEM and TEM analysis.

3. Results and Discussion

3.1. Structural, Surface Property and Thermal Behavior Investigation of the Nanocomposites

Small angle X-ray diffraction (SAXRD) measurements were carried out to examine the structural order of the prepared nanocomposite material. Figure 1A displays the SAXRD patterns of CMK-9 and the $\text{Fe}_3\text{O}_4(x)\text{@C9}$ nanocomposites. As seen in Figure 1A(a), CMK-9 exhibited two peaks related to (211) and (220) planes of the cubic $Ia3d$ space group, revealing its bicontinuous 3D ordered mesoporous structure [16]. The intensity of the major peak decreased after the inclusion of the Fe_3O_4 nanoparticles into CMK-9, as shown in Figure 1A(b–f). The peak intensity continuously decreased with the increase in the amount of Fe_3O_4 NPs in the nanocomposites and completely disappeared for $\text{Fe}_3\text{O}_4(25)\text{@C9}$. The decrease in peak intensity revealed the filling of Fe_3O_4 NPs into the mesopores of CMK-9, which slowly deteriorated the mesoporous structure. When the concentration of Fe_3O_4 was raised to 25 wt.%, the mesopore architecture nearly crumbled due to the volumetric strain developed in the $\text{Fe}_3\text{O}_4(25)\text{@C9}$ nanocomposite system and, hence, the complete disappearance of the peak [35].

The WAXRD patterns of pristine Fe_3O_4 , CMK-9 and $\text{Fe}_3\text{O}_4(x)\text{@C9}$ nanocomposites are shown in Figure 1B. The synthesized pristine Fe_3O_4 nanoparticles exhibited all the characteristic peaks of cubic spinel Fe_3O_4 phases, which matched well with the JCPDS data (JCPDS#19-0629, Figure 1B(a)). The pristine CMK-9 displayed two broad peaks with low intensities at around 2θ values of $14\text{--}32^{\circ}$ and $40\text{--}46^{\circ}$ for (002) and (100) diffraction planes, respectively, of turbostratic carbon, signifying lower graphitization for CMK-9 [36]. The WAXRD patterns of $\text{Fe}_3\text{O}_4(x)\text{@C9}$ with different Fe_3O_4 loadings demonstrated the peaks of both Fe_3O_4 and CMK-9, suggesting the successful formation of nanocomposites (Figure 1B(d–h)). At a lower concentration of 4 wt.%, the peaks corresponding to Fe_3O_4 were not visible in the XRD patterns of $\text{Fe}_3\text{O}_4(4)\text{@C9}$ nanocomposite since most of the Fe_3O_4 nanoparticles were embedded into the mesopores of CMK-9 and possibly elevated the noise level of signals marginally. However, broad peaks of CMK-9 were present in the nanocomposite. With increasing the Fe_3O_4 concentration, the high-intensity peaks started to appear and clearly became visible in the $\text{Fe}_3\text{O}_4(25)\text{@C9}$ nanocomposite with the

maximum Fe_3O_4 loading, exhibiting six peaks for the diffraction planes (111), (220), (311), (400), (511) and (440) of cubic Fe_3O_4 along with the (002) diffraction of CMK-9. The wider diffraction peaks of Fe_3O_4 in the nanocomposites compared to pristine Fe_3O_4 indicated the availability of smaller NPs in the nanocomposites. The reduction in peak intensity and broadening of the peak for (002) diffraction with the increase in the Fe_3O_4 amount revealed the decline of the ordered mesostructure of CMK-9. As CMK-9 possessed bicontinuous ordered mesoporous architecture, it could influence the growth of Fe_3O_4 nanoparticles inside the mesopore frameworks to form smaller-size nanoparticles.

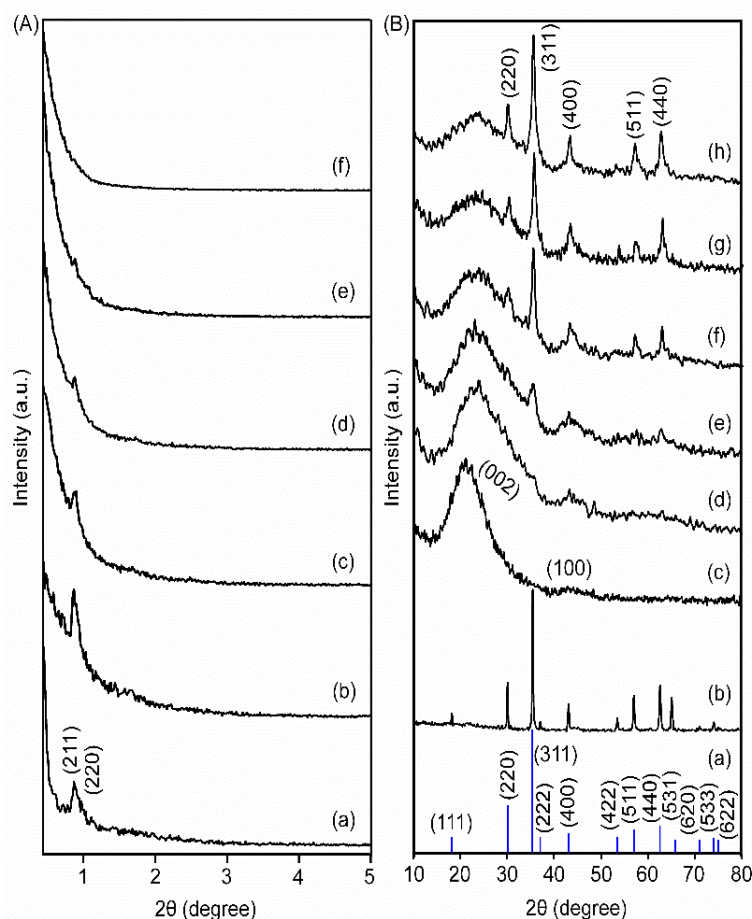


Figure 1. (A) SAXRD patterns of (a) pristine CMK-9, (b) $\text{Fe}_3\text{O}_4(4)@C9$, (c) $\text{Fe}_3\text{O}_4(8)@C9$, (d) $\text{Fe}_3\text{O}_4(13)@C9$, (e) $\text{Fe}_3\text{O}_4(18)@C9$ and (f) $\text{Fe}_3\text{O}_4(25)@C9$ nanocomposites. (B) WAXRD patterns of (a) Fe_3O_4 (JCPDS#19-0629), (b) pristine Fe_3O_4 NPs, (c) CMK-9, (d) $\text{Fe}_3\text{O}_4(4)@C9$, (e) $\text{Fe}_3\text{O}_4(8)@C9$, (f) $\text{Fe}_3\text{O}_4(13)@C9$, (g) $\text{Fe}_3\text{O}_4(18)@C9$ and (h) $\text{Fe}_3\text{O}_4(25)@C9$ nanocomposites.

The nitrogen adsorption/desorption isotherms and pore size variation of CMK-9 and $\text{Fe}_3\text{O}_4(x)@C9$ with varied Fe_3O_4 amounts are displayed in Figure 2. The isotherms demonstrated type IV hysteresis loops according to the IUPAC classification, revealing the mesoporous structure of the materials. The surface area, pore volume and pore size of the materials are presented in Table 1. As seen in Table 1, the CMK-9 exhibited a surface area of $2487 \text{ m}^2 \text{ g}^{-1}$, pore volume of $2.36 \text{ cm}^3 \text{ g}^{-1}$ and bimodal pore size of 3.5 and 5.7 nm. The inner tube of CMK-9 created larger pores with a diameter of 5.7 nm, while the inter-tube generated pores with a diameter of 3.5 nm. After the inclusion of Fe_3O_4 NPs into the CMK-9, the surface area and pore volume of the composite started to decline. The surface areas were estimated to be 1859, 1785, 1654, 1497 and $1312 \text{ m}^2 \text{ g}^{-1}$ for $\text{Fe}_3\text{O}_4(4)@C9$, $\text{Fe}_3\text{O}_4(8)@C9$, $\text{Fe}_3\text{O}_4(13)@C9$, $\text{Fe}_3\text{O}_4(18)@C9$ and $\text{Fe}_3\text{O}_4(25)@C9$, respectively. The corresponding pore volumes were 1.72, 1.66, 1.55, 1.34 and $1.2 \text{ cm}^3 \text{ g}^{-1}$. The surface area and pore volumes were observed to be decreasing with the increase in concentration

of Fe precursor. Meanwhile, the pore size variation was almost similar for CMK-9 and $\text{Fe}_3\text{O}_4(x)\text{@C9}$ nanocomposites. At the time of preparation of the nanocomposite, there was no change in the synthesis condition, for instance, the addition of swelling agents, co-surfactant, salts and Fe_3O_4 precursors into the CMK-9 scaffolds. Moreover, the use of a wet-impregnation process in the synthesis process eliminates the possibility of pore size alteration. However, the filling of mesopores with Fe_3O_4 nanoparticles indeed reduces the pore volume and surface area of the nanocomposites. The observation of hysteresis loops in the $\text{Fe}_3\text{O}_4(x)\text{@C9}$ nanocomposite samples suggested the presence of some unfilled mesopores. These mesopore volumes were advantageous for infiltration with electrolytes, which improved the electrolyte–electrode contact and faster diffusion of charges and provided more redox active sites. In addition, it assisted in cushioning the volume variation of Fe_3O_4 nanoparticles during charge/discharge cycles.

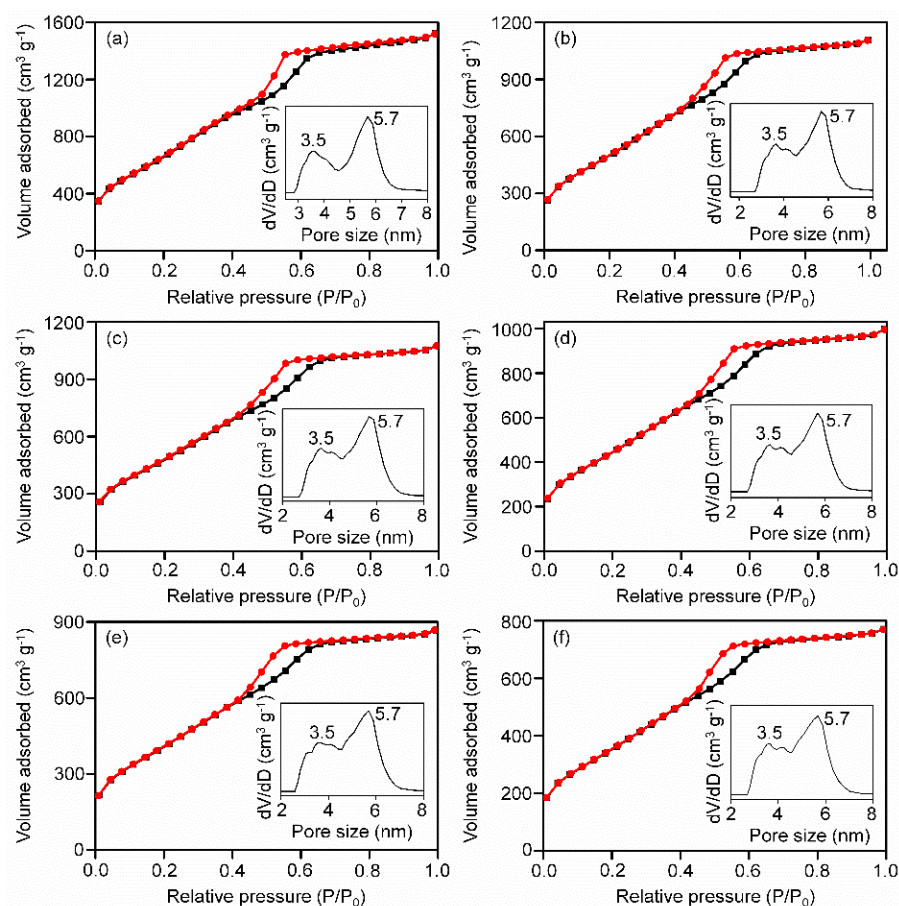


Figure 2. N_2 adsorption/desorption isotherms of (a) pristine CMK-9, (b) $\text{Fe}_3\text{O}_4(4)\text{@C9}$, (c) $\text{Fe}_3\text{O}_4(8)\text{@C9}$, (d) $\text{Fe}_3\text{O}_4(13)\text{@C9}$, (e) $\text{Fe}_3\text{O}_4(18)\text{@C9}$ and (f) $\text{Fe}_3\text{O}_4(25)\text{@C9}$ nanocomposites. Pore size variations are shown in the insets.

Table 1. Textural properties of pristine CMK-9 and $\text{Fe}_3\text{O}_4(x)\text{@C9}$ nanocomposites.

Materials	Surface Area ($\text{m}^2 \text{g}^{-1}$)	Pore Volume ($\text{cm}^3 \text{g}^{-1}$)	Pore Size (nm)
Pristine CMK-9	2487	2.36	3.5, 5.7
$\text{Fe}_3\text{O}_4(4)\text{@C9}$	1859	1.72	3.5, 5.7
$\text{Fe}_3\text{O}_4(8)\text{@C9}$	1785	1.66	3.5, 5.7
$\text{Fe}_3\text{O}_4(13)\text{@C9}$	1654	1.55	3.5, 5.7
$\text{Fe}_3\text{O}_4(18)\text{@C9}$	1497	1.34	3.5, 5.7
$\text{Fe}_3\text{O}_4(25)\text{@C9}$	1312	1.20	3.5, 5.7

Thermogravimetric analysis (TGA) was performed on the nanocomposite samples to measure the portion of Fe_3O_4 in the nanocomposite. Figure 3 shows the TGA thermograms of pristine CMK-9 and $\text{Fe}_3\text{O}_4(x)\text{@C9}$. The weight loss of 1–3 wt.% at a temperature below 150 °C was ascribed to the evaporation of physisorbed and chemisorbed water and trace elements. A major weight reduction was observed between 500 and 670 °C for pristine CMK-9 owing to oxidation of carbon to form CO_2 [37]. Additional heating beyond 670 °C resulted in gross weight reduction for pristine CMK-9. In the case of $\text{Fe}_3\text{O}_4(x)\text{@C9}$ nanocomposites, the thermal stability of the materials was reduced with the introduction of Fe_3O_4 nanoparticles. The major weight loss stage was observed between 360 and 550 °C because of oxidative breakdown of carbon and oxidation of Fe_3O_4 to Fe_2O_3 [38]. The weight loss became stable above 600 °C, and the remaining component was Fe_2O_3 . From the TGA curves and conversion formula ($4\text{Fe}_3\text{O}_4 + \text{O}_2 = 6\text{Fe}_2\text{O}_3$), the amounts of Fe_3O_4 in the nanocomposites were calculated and found to be 4.4, 8.1, 13.3, 18.7 and 25.2 wt.% for $\text{Fe}_3\text{O}_4(4)\text{@C9}$, $\text{Fe}_3\text{O}_4(8)\text{@C9}$, $\text{Fe}_3\text{O}_4(13)\text{@C9}$, $\text{Fe}_3\text{O}_4(18)\text{@C9}$ and $\text{Fe}_3\text{O}_4(25)\text{@C9}$, respectively. Therefore, both theoretically calculated and TGA data showed almost similar amounts of Fe_3O_4 in the nanocomposite.

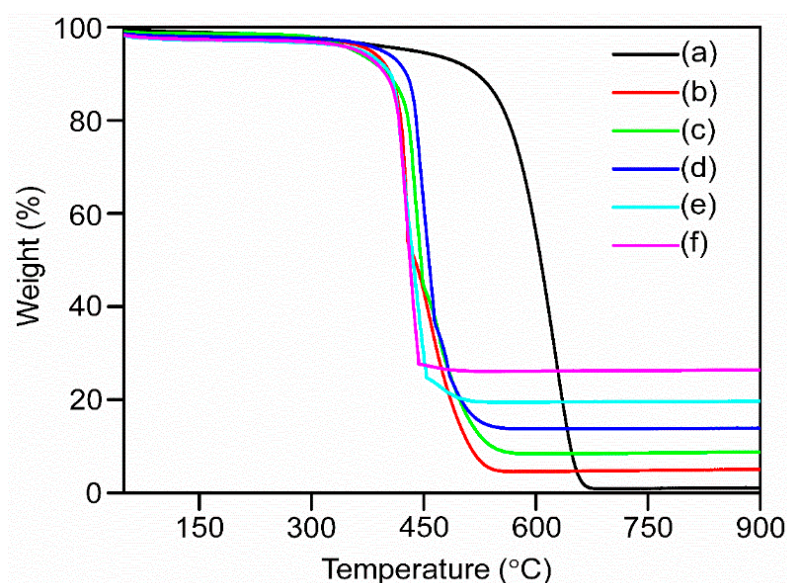


Figure 3. TGA thermograms of (a) pristine CMK-9, (b) $\text{Fe}_3\text{O}_4(4)\text{@C9}$, (c) $\text{Fe}_3\text{O}_4(8)\text{@C9}$, (d) $\text{Fe}_3\text{O}_4(13)\text{@C9}$, (e) $\text{Fe}_3\text{O}_4(18)\text{@C9}$ and (f) $\text{Fe}_3\text{O}_4(25)\text{@C9}$ nanocomposites.

3.2. Morphological and Microstructural Features of the Nanocomposite

The morphological and microstructural analyses of pristine CMK-9 OMC and $\text{Fe}_3\text{O}_4(x)\text{@C9}$ nanocomposites were assessed by TEM and HRTEM analysis. Figure 4 presents the TEM images of pristine CMK-9, $\text{Fe}_3\text{O}_4(4)\text{@C9}$, $\text{Fe}_3\text{O}_4(8)\text{@C9}$, $\text{Fe}_3\text{O}_4(13)\text{@C9}$, $\text{Fe}_3\text{O}_4(18)\text{@C9}$ and $\text{Fe}_3\text{O}_4(25)\text{@C9}$ nanocomposites. The particle-size variation is displayed as an inserted diagram with the respective TEM images of the nanocomposite samples. The mesoporous channels of pristine CMK-9 were obviously seen in Figure 4a. The TEM images of $\text{Fe}_3\text{O}_4(x)\text{@C9}$ nanocomposites with varied Fe_3O_4 amounts are displayed in Figure 4(b–f). It was observed that most of the spherical Fe_3O_4 nanoparticles were homogeneously distributed within the mesopores of CMK-9 scaffolds. From particle-size variation curves, it was clear that the average size of Fe_3O_4 nanoparticles grew with the increase in the Fe_3O_4 precursor concentration. The nanoparticle sizes were measured to be 2.61, 2.94, 3.55, 3.94 and 4.87 nm for $\text{Fe}_3\text{O}_4(4)\text{@C9}$, $\text{Fe}_3\text{O}_4(8)\text{@C9}$, $\text{Fe}_3\text{O}_4(13)\text{@C9}$, $\text{Fe}_3\text{O}_4(18)\text{@C9}$ and $\text{Fe}_3\text{O}_4(25)\text{@C9}$, respectively. In addition, a few relatively large Fe_3O_4 nanoparticles were observed on the surface of CMK-9 OMC at higher Fe_3O_4 precursor concentrations. The high-resolution TEM (HRTEM) image of $\text{Fe}_3\text{O}_4(13)\text{@C9}$ in Figure 5a exhibited lattice spacing of 0.25 and 0.29 nm for (311) and (220) planes of crystalline cubic Fe_3O_4 , respec-

tively [34]. This suggested the efficient encapsulation of Fe_3O_4 NPs into CMK-9 scaffolds. The selected area electron diffraction (SAED) displayed in Figure 5b revealed distinct circular designs that matched exactly with the (220), (311), (400) and (440) lattice planes of cubic Fe_3O_4 , suggesting the growth of well crystallized Fe_3O_4 NPs within the $\text{Fe}_3\text{O}_4(13)\text{@C9}$ nanocomposite [39].

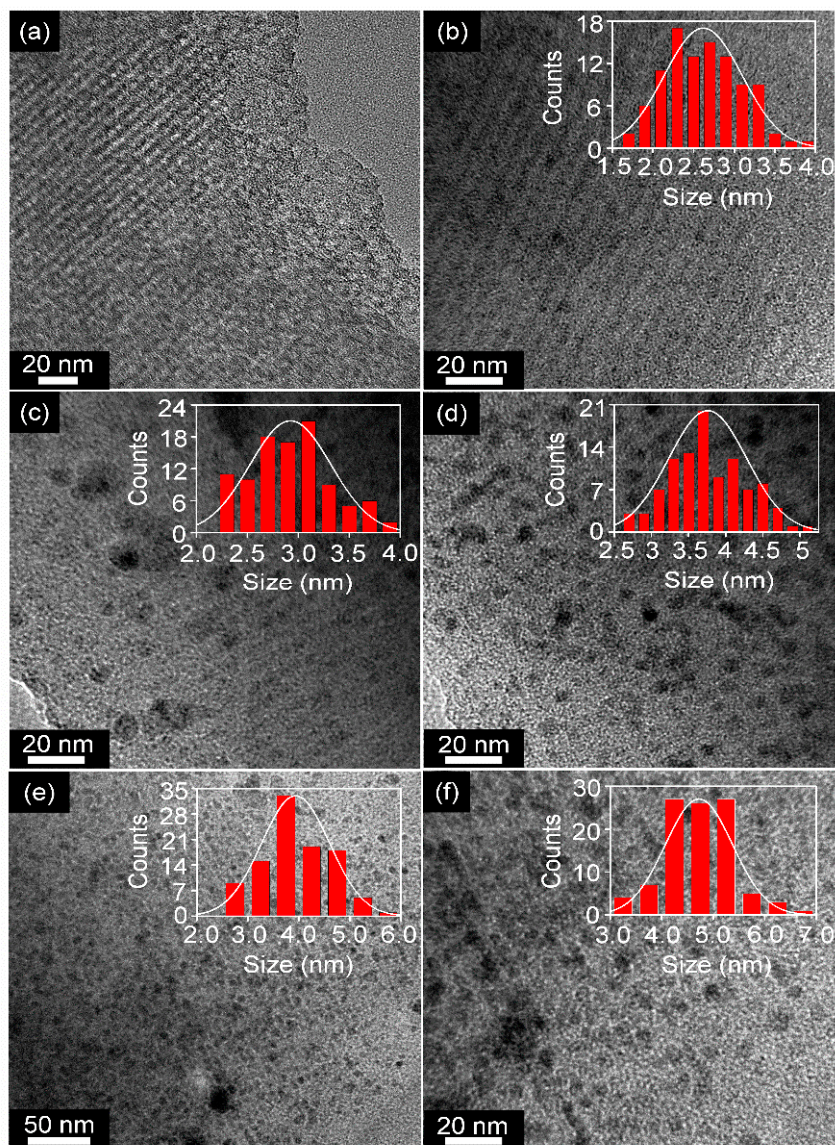


Figure 4. TEM images of (a) pristine CMK-9, (b) $\text{Fe}_3\text{O}_4(4)\text{@C9}$, (c) $\text{Fe}_3\text{O}_4(8)\text{@C9}$, (d) $\text{Fe}_3\text{O}_4(13)\text{@C9}$, (e) $\text{Fe}_3\text{O}_4(18)\text{@C9}$ and (f) $\text{Fe}_3\text{O}_4(25)\text{@C9}$ nanocomposites.

The energy-dispersive X-ray spectroscopy (EDX) elemental mapping validated the presence of Fe, C and O elements in the nanocomposite (Figure 5c–f). The mapping images clearly suggested the uniform distribution of Fe_3O_4 nanoparticles in the $\text{Fe}_3\text{O}_4(13)\text{@C9}$ nanocomposite. These results indicate that CMK-9 OMC can restrict the aggregation of Fe_3O_4 nanoparticles mostly by confining them inside the mesopores. This may lead to effective buffering of the volume variation of Fe_3O_4 nanoparticles throughout the charging and discharging processes and also assists in the movements of electrons and ions.

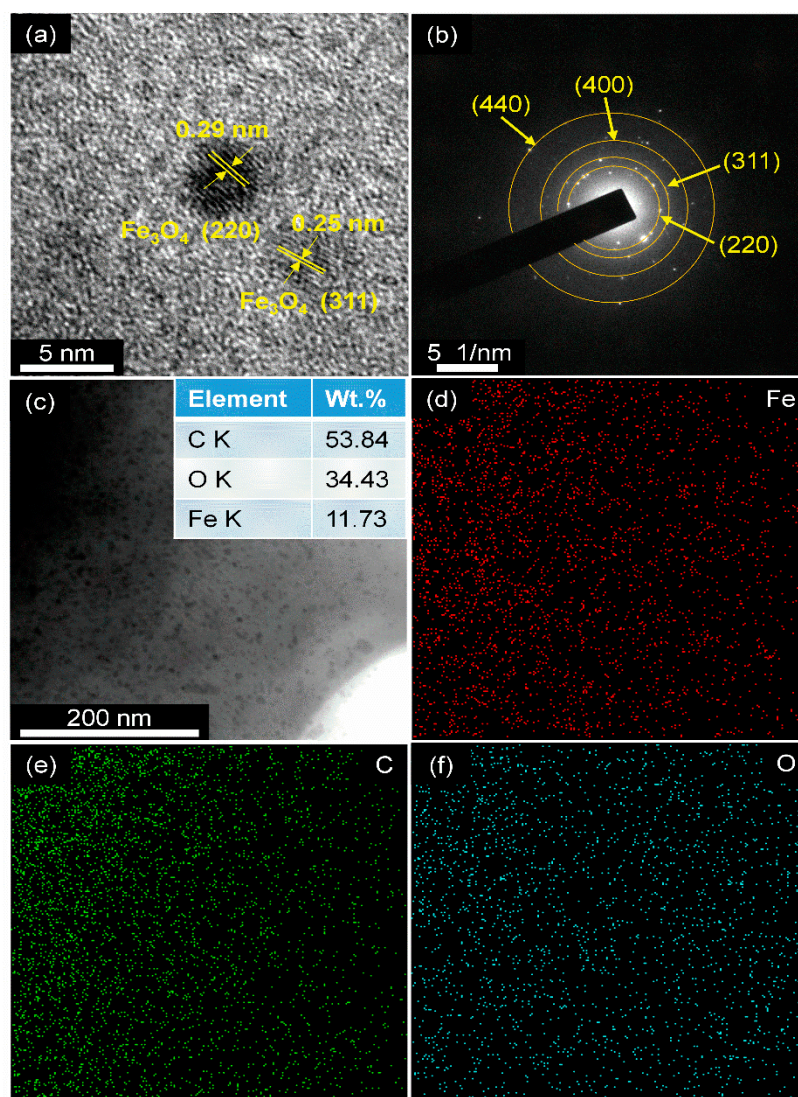


Figure 5. (a) HRTEM image of Fe₃O₄(13)@C9 with d-spacing, (b) SAED pattern, (c–f) bright-field TEM image with EDX elemental mapping of Fe₃O₄(13)@C9.

3.3. Analysis of Surface States and Degree of Graphitization

X-ray photoelectron spectroscopy (XPS) was performed to explore the surface electronic states and chemical composition of Fe₃O₄(x)@C9 nanocomposite. Figure 6 shows the typical survey and high-resolution XPS spectra for the Fe₃O₄(13)@C9 nanocomposite. The survey spectrum in Figure 6a exhibited three distinct peaks accorded with Fe 2p, O 1s and C 1s, suggesting the presence of Fe, O and C in Fe₃O₄(13)@C9 and corroborated the outcome acquired from EDX. The higher magnification XPS spectrum of Fe 2p displayed two main peaks at 711.5 and 725.4 eV, which were the characteristics of Fe 2p_{3/2} and Fe 2p_{1/2} electronic states of Fe₃O₄ (Figure 6b) [21]. Deconvolution of the two main peaks generated peaks for Fe²⁺ and Fe³⁺ oxidation states, as Fe₃O₄ consisted of these two states. The fitting peaks at 711.4 and 725.4 eV corresponded to Fe 2p_{3/2} and Fe 2p_{1/2} electronic states of Fe²⁺, while the peaks at 713.5 and 728.4 eV were assigned to Fe 2p_{3/2} and Fe 2p_{1/2} of Fe³⁺ oxidation state, respectively [40]. The peaks obtained at 719.9 and 734.2 eV were referred to as shake-up satellite peaks of the Fe²⁺ oxidation state [41]. The higher magnification O 1s spectrum was deconvoluted into four peaks, as presented in Figure 6c. The peak at 530.4 eV was assigned to Fe–O binding of Fe₃O₄ [42]. The peak that appeared at 531.6 eV was ascribed to the Fe–O–C bonding [20]. The presence of Fe–O–C bond suggested confinement of Fe₃O₄ NPs in the interior of the mesopores of CMK-9 scaffolds. Confine-

ment of Fe_3O_4 nanoparticles in the mesopores prevents aggregation of the particles as well as assists in the rapid charge and mass transfer during the lithiation/delithiation process. The peaks at 532.5 and 534 eV were related to C=O and C-O bindings of carbonyl, carboxyl and hydroxyl groups [20].

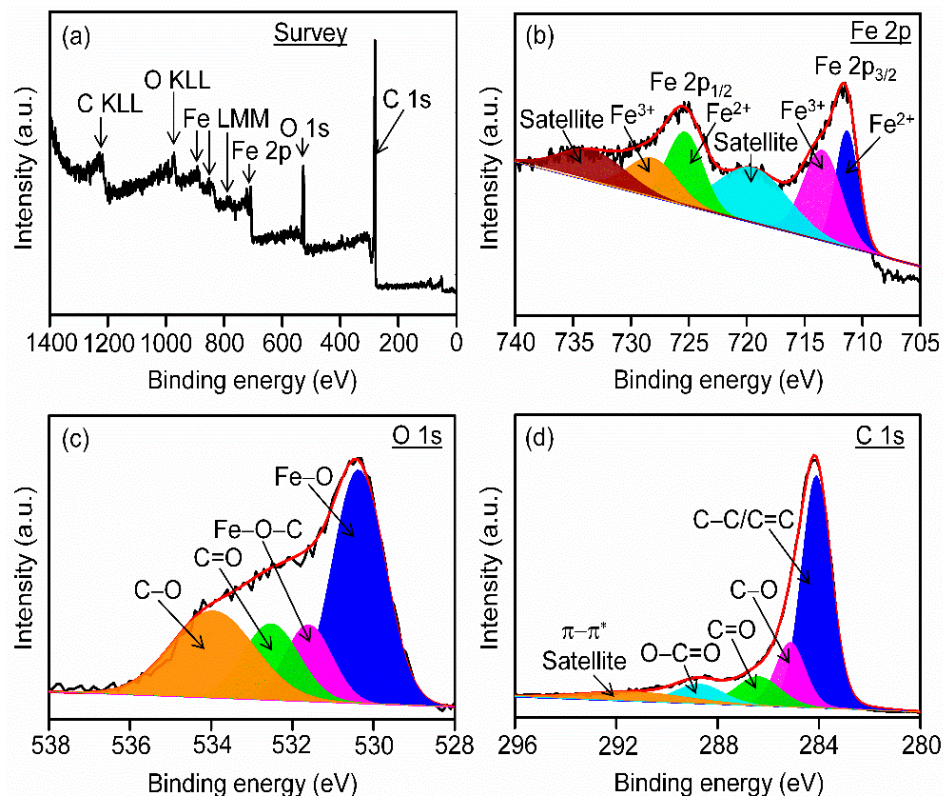


Figure 6. (a) Survey spectrum and higher magnification XPS spectra of (b) Fe 2p, (c) O 1s and (d) C 1s for $\text{Fe}_3\text{O}_4(13)@C9$ nanocomposite.

Deconvolution of C 1s peak presented five peaks, as shown in Figure 6d. The main high-intensity peak at 284.1 eV was ascribed to C-C (sp^2 hybrid) bonding from the graphitic carbon of CMK-9. The peaks at 285.1, 286.4 and 288.7 eV were allocated to hydroxyl and epoxy (C-O), carbonyl (C=O) and carboxyl (O-C=O) groups, respectively, suggesting the presence of these functional groups on the surface of CMK-9 [43,44]. The peak at 291.7 eV was connected to the π - π^* shake up satellite [43]. The appearance of such functional groups might have influenced the surface properties of $\text{Fe}_3\text{O}_4(13)@C9$ nanocomposite substantially.

Raman spectra were acquired to evaluate the phase and graphitization degree of the nanocomposites. The Raman spectra of pristine CMK-9 and $\text{Fe}_3\text{O}_4(x)@C9$ nanocomposites are displayed in Figure 7. All the spectra exhibited two distinctive carbon peaks at about 1310 and 1574 cm^{-1} for defect or disordered (D band) and in-plane sp^2 -hybridized graphitic carbon (G band, E_{2g} photons), respectively [45]. The degree of graphitization of carbonaceous materials can be measured from the intensity ratio of the D band and G band (I_D/I_G). A lower I_D/I_G value reveals more graphitization [46]. The relative I_D/I_G values were calculated to be 0.99 for pristine CMK-9 and 1.001 for all the $\text{Fe}_3\text{O}_4(x)@C9$ nanocomposites. The values of I_D/I_G close to unity suggested the amorphous nature of carbon with a few layers of graphitic phases. Therefore, the current nanocomposites display an acceptable degree of graphitization, which may help to achieve decent electronic conductivity and, hence, improved electrochemical performances.

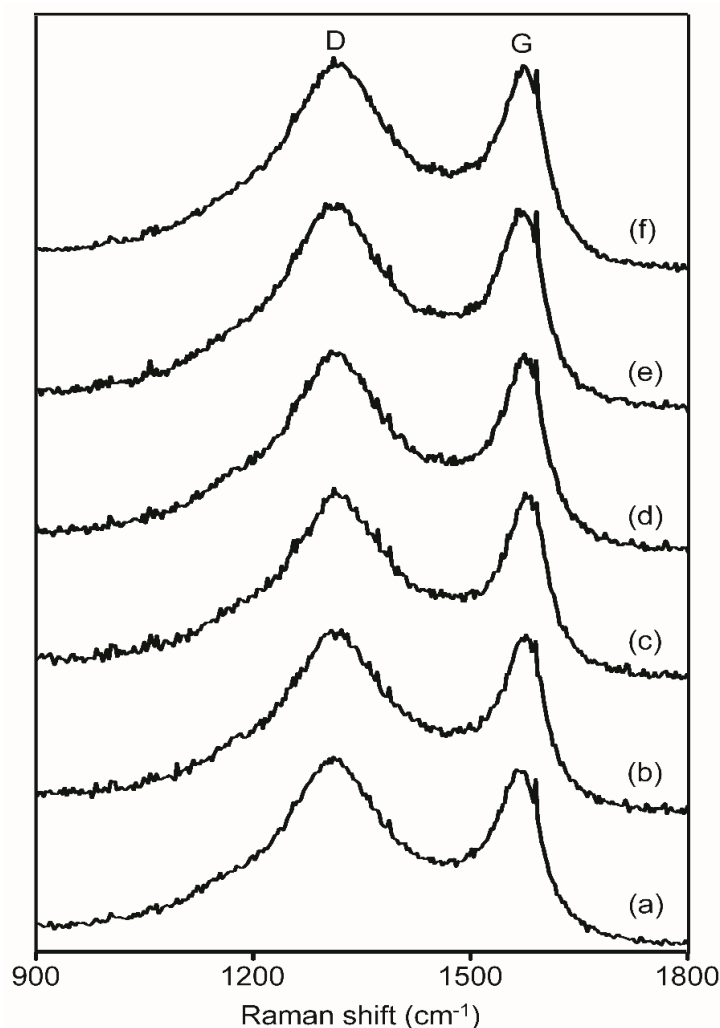
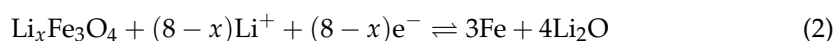


Figure 7. Raman spectra of (a) pristine CMK-9, (b) $\text{Fe}_3\text{O}_4(4)\text{@C9}$, (c) $\text{Fe}_3\text{O}_4(8)\text{@C9}$, (d) $\text{Fe}_3\text{O}_4(13)\text{@C9}$, (e) $\text{Fe}_3\text{O}_4(18)\text{@C9}$ and (f) $\text{Fe}_3\text{O}_4(25)\text{@C9}$ nanocomposites.

3.4. Electrochemical Performances of the Nanocomposites

Cyclic voltammetry (CV) measurements of the $\text{Fe}_3\text{O}_4(x)\text{@C9}$ nanocomposite anodes were carried out to analyze the electrochemical responses during the charging and discharging processes. Figure 8 shows the CV curves of pristine CMK-9 and $\text{Fe}_3\text{O}_4(x)\text{@C9}$ nanocomposites for the first 10 cycles in the potential range of 0.01 to 3.0 V at a scan rate of 0.1 mV s^{-1} . As observed from the figure, the first cycle CV curve varied from the rest of the cycles owing to the growth of the solid electrolyte interface (SEI) layer [47]. The first cycle CV curve of pristine CMK-9 demonstrated a cathodic peak at around 0.5 V that was ascribed to the electrolyte decomposition and generation of SEI (Figure 8a) [48]. The pointed cathodic peak at 0.01 V corresponded to the lithium inclusion into CMK-9 scaffolds. The small anodic peak observed at about 1.28 V could be ascribed to the limited deposition of SEI [49]. In the case of $\text{Fe}_3\text{O}_4(x)\text{@C9}$ nanocomposite anodes, the first cycle CV curves showed two reduction peaks around 0.54 and 0.98 V due to the SEI layer formation and/or inclusion of Li^+ into the Fe_3O_4 lattices and reduction of $\text{Li}_x\text{Fe}_3\text{O}_4$ into Fe and Li_2O [20].



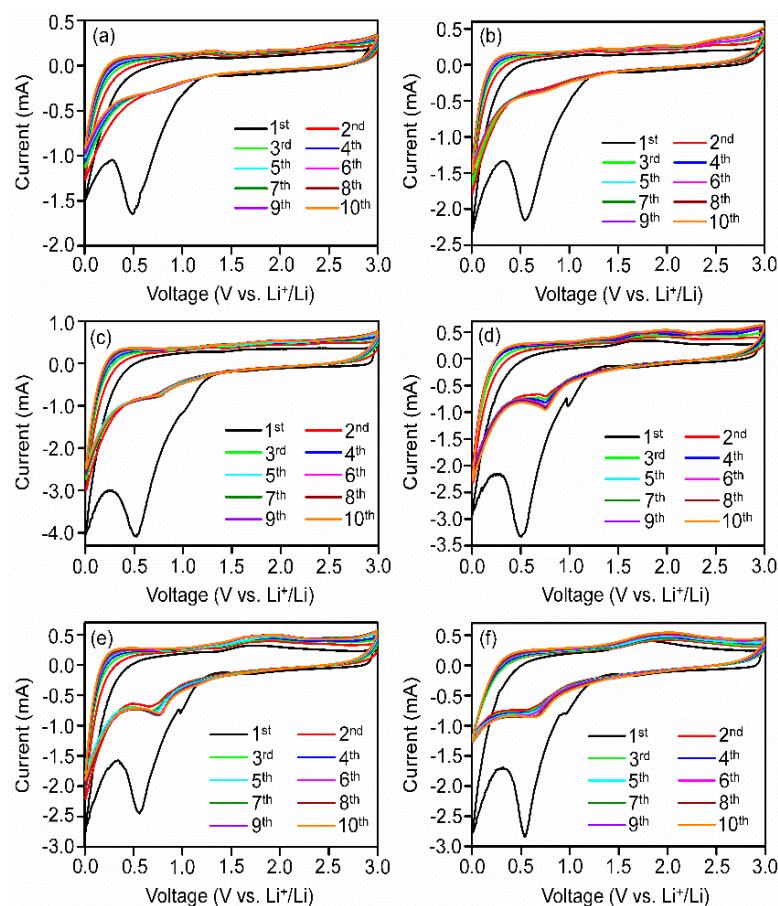


Figure 8. CV curves of (a) pristine CMK-9, (b) $\text{Fe}_3\text{O}_4(4)\text{@C9}$, (c) $\text{Fe}_3\text{O}_4(8)\text{@C9}$, (d) $\text{Fe}_3\text{O}_4(13)\text{@C9}$, (e) $\text{Fe}_3\text{O}_4(18)\text{@C9}$ and (f) $\text{Fe}_3\text{O}_4(25)\text{@C9}$ nanocomposite anodes.

These two peaks were shifted to higher voltages of 0.76 and 1.16 V in the successive cycles with reduced intensities, confirming the reversibility of the reaction processes. The sharp reduction peak at around 0.01 V was also observed for the $\text{Fe}_3\text{O}_4(x)\text{@C9}$ nanocomposite anodes as a result of partial Li^+ insertion into the CMK-9 matrix [50]. In the anodic sweep, two peaks were detected around 1.6 and 1.98 V for the entire nanocomposite anodes attributed to the continuous oxidation of Fe^0 to Fe^{2+} and Fe^{3+} , successively [38]. Noticeably, the almost overlapping of CV curves from the third cycle onwards suggested the good reversibility of charge–discharge reactions of $\text{Fe}_3\text{O}_4(x)\text{@C9}$ nanocomposite electrodes.

To explore the lithium storage capability, the charge–discharge profiles of pristine CMK-9 and $\text{Fe}_3\text{O}_4(x)\text{@C9}$ anodes were acquired at a current rate of 100 mA g^{-1} for initial 10 cycles and presented in Figure 9. For the CMK-9 anode, the initial discharge and charge capacities of 2931.4 and $1647.5 \text{ mA h g}^{-1}$, successively, were observed with an initial coulombic efficiency (CE) value of 56.2%. A voltage plateau was observed between 0.7 and 1.0 V at the beginning of the discharge cycle owing to the decomposition of electrolyte and generation of the SEI layer [49]. For the $\text{Fe}_3\text{O}_4(x)\text{@C9}$ nanocomposite anode, the electrodes delivered first cycle discharge capacities of 2918.21, 2825.58, 3513.21, 2742.74 and $2610.23 \text{ mA h g}^{-1}$ and charge capacities of 1809.29, 1836.63, 2494.67, 1727.93 and $1566.14 \text{ mA h g}^{-1}$ for $\text{Fe}_3\text{O}_4(4)\text{@C9}$, $\text{Fe}_3\text{O}_4(8)\text{@C9}$, $\text{Fe}_3\text{O}_4(13)\text{@C9}$, $\text{Fe}_3\text{O}_4(18)\text{@C9}$ and $\text{Fe}_3\text{O}_4(25)\text{@C9}$, respectively, with corresponding initial CE values of 61.9, 65, 71, 63 and 60%. The irreversible capacity loss was mainly directed to the generation of the SEI layer, the high surface area of CMK-9 that suppressed the reversible faradic reactions, and the entrapment of a part of Li-ions inside the mesopores of CMK-9 [10,51]. The voltage plateau spanning over 0.78 to 1.3 V in the beginning discharge cycle was ascribed to the generation of the SEI layer and reduction of $\text{Li}_x\text{Fe}_3\text{O}_4$ into Fe and Li_2O , which corroborated the CV

results [10]. In the charge process, the slope observed in the first cycle around 1.1–1.8 V corresponded to the oxidation of Fe to Fe²⁺ and Fe³⁺ [10]. The charge–discharge curves were nearly overlapped from the fourth cycle onwards, indicating superior reversibility and strong electrochemical performances of the Fe₃O₄(*x*)@C9 nanocomposite anodes.

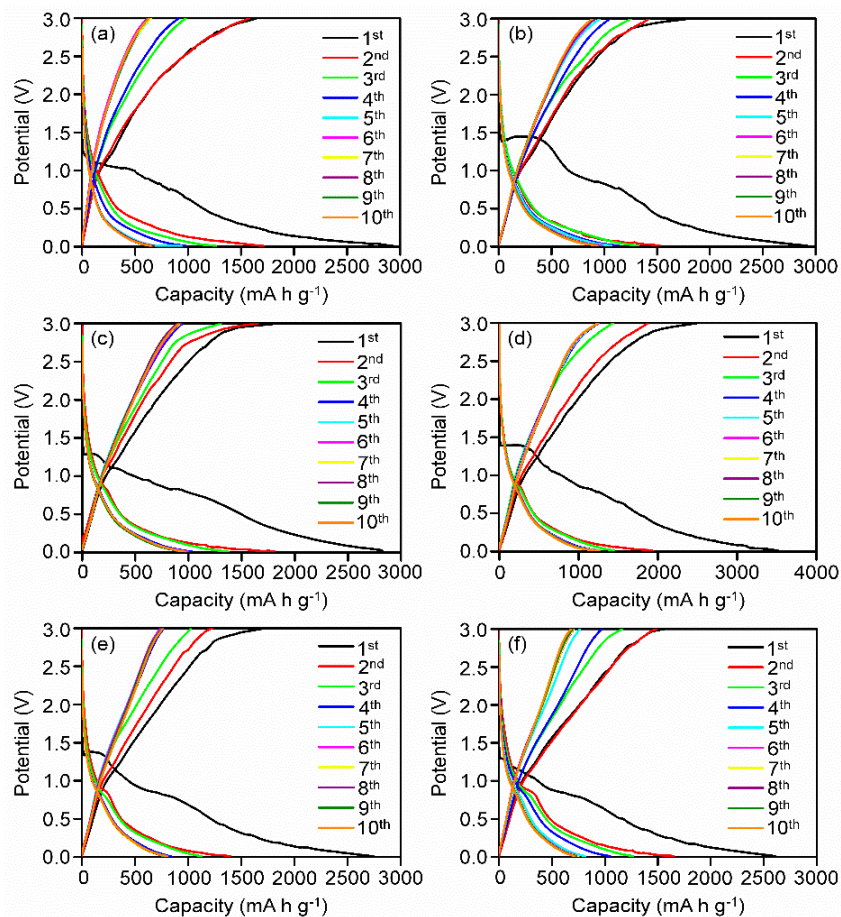


Figure 9. Charge–discharge profiles of (a) pristine CMK-9, (b) Fe₃O₄(4)@C9, (c) Fe₃O₄(8)@C9, (d) Fe₃O₄(13)@C9, (e) Fe₃O₄(18)@C9 and (f) Fe₃O₄(25)@C9 nanocomposite anodes.

The electrochemical stabilities of the electrodes were tested by cycling at different current rates. Figure 10A depicts the discharge capacities of Fe₃O₄(*x*)@C9 and CMK-9 electrodes at current densities of 100, 200, 500, 1000, 2000 and again at 100 mA g^{−1}. The average discharge capacities of 1258, 1123, 933, 728, 450 and 1253 mA h g^{−1} were accomplished for the Fe₃O₄(13)@C9 anode at current densities of 100, 200, 500, 1000, 2000 and again at 100 mA g^{−1}, respectively. Although the capacity was slightly lower after 50 cycles at the same current rate of 100 mA g^{−1}, the Fe₃O₄(13)@C9 anode retained over 99% capacity after 60 cycles, validating the durability of the anode despite cycling at high rates. Remarkably, the Fe₃O₄(13)@C9 anode delivered a capacity greater than the theoretical capacity of Fe₃O₄ (~924 mA h g^{−1}) at current densities from 100 to 500 mA g^{−1}. On the other hand, the discharge capacities of 935, 971, 821, 713 and 650 mA h g^{−1} were attained for Fe₃O₄(4)@C9, Fe₃O₄(8)@C9, Fe₃O₄(18)@C9, Fe₃O₄(25)@C9 and CMK-9, respectively, at a current rate of 100 mA g^{−1}. At 1000 mA g^{−1}, the respective discharge capacities were 477, 563, 450, 356 and 326 mA h g^{−1}. From these results, it is suggested that Fe₃O₄(13)@C9 has delivered remarkable rate capability and stability compared to the other nanocomposite electrode samples.

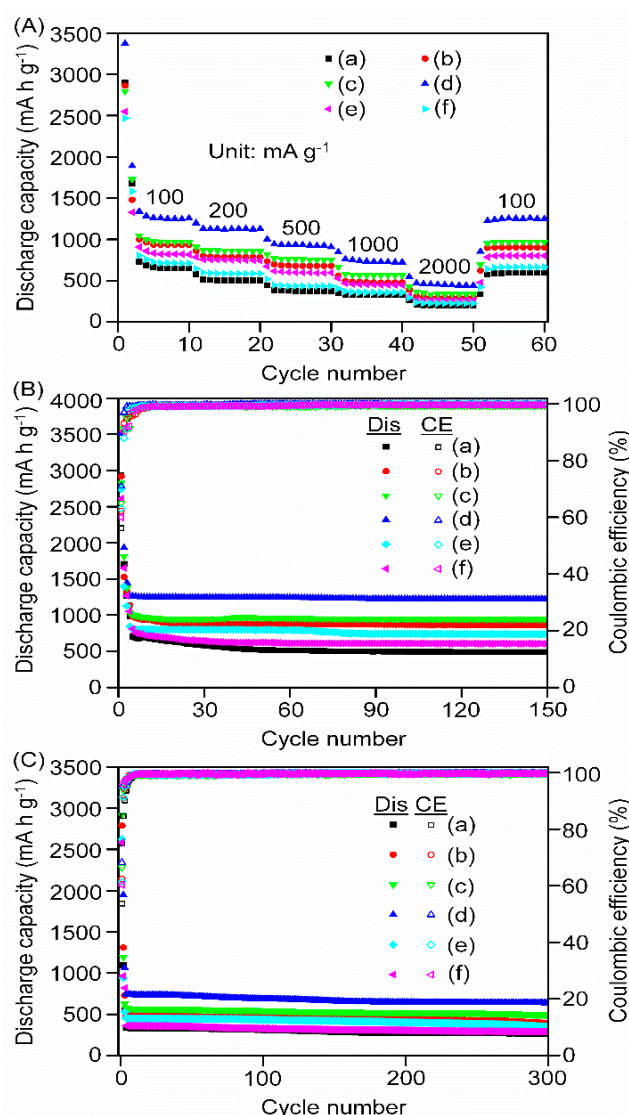


Figure 10. (A) Rate capability and cycle performances at current rates of (B) 100 and (C) 1000 mA g⁻¹ for (a) pristine CMK-9, (b) Fe₃O₄(4)@C9, (c) Fe₃O₄(8)@C9, (d) Fe₃O₄(13)@C9, (e) Fe₃O₄(18)@C9 and (f) Fe₃O₄(25)@C9 nanocomposite anodes.

To explore the cycle stability for a longer duration, the cycle performances of Fe₃O₄(*x*)@C9 nanocomposite electrodes and pristine CMK-9 were measured at current rates of 100 and 1000 mA g⁻¹. Figure 10B depicts the long-time cycle performances of Fe₃O₄(*x*)@C9 and pristine CMK-9 at a current rate of 100 mA g⁻¹. The Fe₃O₄(13)@C9 anode delivered the beginning cycle discharge capacity of 3513.21 mA h g⁻¹ that fell to 1262.76 mA h g⁻¹ in the fourth cycle mainly because of the formation of the SEI layer. After the 4th cycle, the rate of fall in capacity decreased, and the electrode supplied a discharge capacity of 1222.11 mA h g⁻¹ after 150 cycles, thus retaining 96.8% capacity as compared to the 4th cycle. It is worth mentioning that the capacity after 150 cycles is still greater than the theoretical capacity of Fe₃O₄ (924 mA h g⁻¹). On the other hand, the Fe₃O₄(4)@C9, Fe₃O₄(8)@C9, Fe₃O₄(18)@C9 and Fe₃O₄(25)@C9 nanocomposite anodes delivered the 4th cycle discharge capacities of 1136.31, 1033.08, 842.4 and 1050.4 mA h g⁻¹ and the 150th cycle discharge capacities of 864.92, 945.67, 736.17 and 604.38 mA h g⁻¹, successively, with corresponding retention capacity of 76.1, 91.5, 87.4 and 57.5%. In contrast, the pristine CMK-9 supplied the 4th cycle discharge capacity of 978.8 mA h g⁻¹, which was reduced to 490.15 mA h g⁻¹ after 150 cycles with a retention capacity of only 50.1%. It was observed that the discharge capacity increased with the rise in the Fe₃O₄ loading in the beginning

and achieved the maximum for Fe₃O₄(13)@C9 nanocomposite. However, the discharge capacity started to decrease for Fe₃O₄(18)@C9 and Fe₃O₄(25)@C9 nanocomposites with higher Fe₃O₄ loadings. Clearly, more Fe₃O₄ particles would form at higher concentrations, and thus, some particles were probably located on the surface of CMK-9 OMC instead of the mesopores. Therefore, particles on the surface may grow larger due to the lack of confinement effect or particle aggregation than the encapsulated particles inside the mesopores. TEM observation also suggested a larger average particle size for the nanocomposites at higher Fe₃O₄ concentrations. The larger size of Fe₃O₄ nanoparticles slowed down the diffusion of charge and mass transfer, resulting in a decrease in capacity. The initial CE values for Fe₃O₄(4)@C9, Fe₃O₄(8)@C9, Fe₃O₄(13)@C9, Fe₃O₄(18)@C9, Fe₃O₄(25)@C9 and pristine CMK-9 were found to be 61.9, 65, 71, 63, 60 and 56.2%, respectively, which gradually improved with the increase in cycle numbers. The entire anodes upheld CE values of more than 99% from 10 to 150 cycles, suggesting superior reversible capacity.

The cycle performances of Fe₃O₄(*x*)@C9 nanocomposite and pristine CMK-9 for a longer duration were determined as well at a higher current rate of 1000 mA g⁻¹, and the results were presented in Figure 10C. The beginning cycle discharge capacities of 2787.52, 2913.94, 3254.87, 2623.69, 2584.49 and 2575.79 mA h g⁻¹ were attained for Fe₃O₄(4)@C9, Fe₃O₄(8)@C9, Fe₃O₄(13)@C9, Fe₃O₄(18)@C9, Fe₃O₄(25)@C9 and pristine CMK-9, respectively, which dropped to 489.33, 574.66, 749.16, 452.15, 361.78 and 333.93 mA h g⁻¹ after the fourth cycle. The reduction in capacity in the initial cycles was mainly attributed to the SEI layer formation on the electrodes. From the 4th cycle onwards, the discharge capacities slowly became steady and delivered the corresponding discharge capacity values of 394.34, 494.71, 636.98, 350.33, 287.84 and 264.14 mA h g⁻¹ after 300 cycles. Thus, the Fe₃O₄(4)@C9, Fe₃O₄(8)@C9, Fe₃O₄(13)@C9, Fe₃O₄(18)@C9, Fe₃O₄(25)@C9 and pristine CMK-9 electrodes could retain capacities of 80.6, 86.1, 85, 77.5, 79.6 and 79.1% after 300 cycles to that of the 4th cycle capacity. For comparison, the cycle performance of pristine Fe₃O₄ NPs was investigated at a current rate of 1000 mA g⁻¹ and the results are shown in Figure S1 (Supplementary Material). The Fe₃O₄ NPs provided the initial cycle discharge capacity of 619.51 mA h g⁻¹, which declined to 430.49 mA h g⁻¹ in the second cycle and 301.39 mA h g⁻¹ in the fourth cycle. Although the rate of capacity decrease was slower after the 4th cycle, the discharge capacity continuously declined and offered a discharge capacity of 177.1 mA h g⁻¹ after 100 cycles, thus retaining 58.7% capacity in comparison to that of the 4th cycle. However, the discharge capacity rapidly decreased after 100 cycles and provided a discharge capacity of 60.14 mA h g⁻¹ after 300 cycles. This resulted in a retention capacity of just 20% in comparison to the fourth cycle. Larger particle sizes of Fe₃O₄ (~51 nm from WAXRD measurements, not shown here) and particle pulverization in the course of charging and discharging mainly contributed to the reduction of capacity for the pristine Fe₃O₄ NP anode. The initial CE values of 62.4, 66.5, 68.2, 61.3, 60.3 and 53.7% were obtained for Fe₃O₄(4)@C9, Fe₃O₄(8)@C9, Fe₃O₄(13)@C9, Fe₃O₄(18)@C9, Fe₃O₄(25)@C9 and pristine CMK-9 electrodes, respectively, at a current rate of 1000 mA g⁻¹. The CE values enhanced incessantly following the first cycle and attained above 99% after a few cycles. It maintained almost similar values for the rest of the cycles, with values of above 99.5% around 300 cycles. The results indicated excellent reversibility of the electrode capacities despite the use of a higher current rate. The discharge capacities of the present Fe₃O₄(13)@C9 electrode and other Fe₃O₄-based composite electrodes reported in the literature are summarized in Table S1 (Supplementary Material) for comparison purposes [10,13,18–21,34,38,44,50,52–57]. Overall, the discharge capacities of the present Fe₃O₄(13)@C9 electrode were greater or almost similar to the other reported Fe₃O₄-based composite electrodes.

To explore the kinetic characteristics, electrochemical impedance spectroscopy (EIS) of pristine CMK-9 and Fe₃O₄(*x*)@C9 nanocomposite anodes was measured after 100 charging and discharging cycles. As displayed in Figure S2 (Supplementary Material), the EIS diagrams exhibited a depressed semicircle in the high-frequency range and a diagonal line in the low-frequency section, respectively. The equivalent circuit model is presented

in Figure S2d (Supplementary Material) as an inset. The high-frequency intercept of the semicircle represents the electrolyte resistance (R_e), while surface (R_s) and charge transfer resistance (R_{ct}) were provided by the high- to medium-frequency semicircle. Surface capacitance is designated as C_s , while C_{dl} represents double-layer capacitance. The diagonal line denotes the Warburg impedance (Z_w) that is associated with the diffusion process of Li-ions [58,59]. The values of R_{ct} were calculated to be 41.4, 35.6, 28.5, 20.3, 28.4 and 32.4 Ω for pristine CMK-9, Fe₃O₄(4)@C9, Fe₃O₄(8)@C9, Fe₃O₄(13)@C9, Fe₃O₄(18)@C9 and Fe₃O₄(25)@C9, respectively. The lower value of R_{ct} for Fe₃O₄(13)@C9 suggested improved electronic conductivity and charge transport.

To demonstrate the Li⁺-ion mobilities, the lithium diffusion coefficients of the materials were estimated from the following equations.

$$D_{Li^+} = \frac{R^2 T^2}{2A^2 n^4 F^4 C^2 \sigma_w^2} \quad (3)$$

$$Z_{re} = R_e + R_{ct} + \sigma_w \omega^{-1/2} \quad (4)$$

where R , T , A , n , F , C and σ_w denote the gas constant (8.314 J mol⁻¹ K⁻¹), the temperature in K, electrode area, number of transferred electrons, Faraday constant, lithium-ions concentration and Warburg factor, respectively. Warburg factor is linked to the real part of the impedance according to Equation (4), where ω indicates the angular frequency. The Z' vs. $\omega^{-1/2}$ graph was drawn from the EIS data and displayed in Figure S3 (Supplementary Material). The slope of the curves provided the σ_w and hence the Li-diffusion coefficients were evaluated using Equation (3) and the values of 5.7×10^{-14} , 7.5×10^{-14} , 1.3×10^{-13} , 2.8×10^{-13} , 7.7×10^{-14} and 5.6×10^{-14} cm² s⁻¹ for pristine CMK-9, Fe₃O₄(4)@C9, Fe₃O₄(8)@C9, Fe₃O₄(13)@C9, Fe₃O₄(18)@C9 and Fe₃O₄(25)@C9, respectively, were obtained. The higher lithium diffusion coefficient for Fe₃O₄(13)@C9 in comparison to other nanocomposite compositions suggested excellent electrochemical performance of the Fe₃O₄(13)@C9 anode.

Based on the above results, the remarkable electrochemical performances of the Fe₃O₄(13)@C9 anode with higher than theoretical capacity might be ascribed to the combined effects of certain important factors. First of all, the capacity contribution from CMK-9 OMC. The substantial number of interconnected mesopores and voids in CMK-9 provided additional spaces to store extra lithium ions that contributed to the enhancement of the capacity. Moreover, the interconnected carbon network with considerable mesopores and higher surface area facilitated the infiltration of electrolytes into the mesopores and thus expedited the mass transfer and favorably enhanced the electrode/electrolyte contact with swift ion diffusion. It also offered several active sites for Li⁺ intercalation/deintercalation for higher capacity. Moreover, the CMK-9 scaffold acted as a buffer to accommodate the Fe₃O₄ nanoparticles efficiently inside the mesopores during the volume change due to the Li⁺ intercalation/deintercalation processes. The mesopores also restricted the aggregation of the nanoparticles, resulting in better cycle life and rate capability. Additionally, the interconnected structure of CMK-9 functioned as the conductive backbone for the electron transport that assisted in lowering the internal resistance and improving the electronic conductivity of the electrode. Secondly, the synergistic effect between Fe₃O₄ nanoparticles and CMK-9 associated with the structure and storage of lithium-ions was beneficial for attaining higher capacity for the nanocomposite anode. Well-distributed Fe₃O₄ nanoparticles within the mesopores of CMK-9 boosted the electrode/electrolyte contacts and avoided aggregation and volume change problems, which resulted in better capacity and long-term cycle stability. Finally, the higher lithium diffusion coefficient for Fe₃O₄(13)@C9 (2.8×10^{-13} cm² s⁻¹) anode in comparison to other nanocomposite compositions facilitated superior electrochemical performances. In addition, the size and concentration of Fe₃O₄ nanoparticles affected the electrochemical performances. Although the Fe₃O₄ particle sizes in Fe₃O₄(4)@C9 and Fe₃O₄(8)@C9 (2.6 nm and 2.9 nm) were smaller than Fe₃O₄(13)@C9 (3.5 nm), the lower concentration of Fe₃O₄ affected their specific capacities

negatively. On the other hand, the higher Fe_3O_4 concentration in the $\text{Fe}_3\text{O}_4(18)@C9$ and $\text{Fe}_3\text{O}_4(25)@C9$ electrodes caused the development of a few aggregated nanoparticles on the surface of CMK-9 rather than confined within the mesopores, leading to larger particle sizes (3.9 nm and 4.8 nm) for these two electrodes with inferior capacities. Therefore, all the aforementioned factors functioned synergistically to achieve excellent specific capacity, rate capability and longer steady cycle life for the $\text{Fe}_3\text{O}_4(13)@C9$ electrode in LIBs.

3.5. Post-Cycle Evaluation of the Nanocomposite Anode

The morphology and microstructure of the cycled $\text{Fe}_3\text{O}_4(13)@C9$ electrode were examined to ascertain the changes that might be occurred during the charge–discharge cycles. Figure 11 displays the SEM, TEM, SAED pattern and EDX elemental mapping of the $\text{Fe}_3\text{O}_4(13)@C9$ anode after 100 charge–discharge cycles. As seen in the SEM images in Figure 11a,b, the morphology of the cycled electrode was slightly altered compared to the uncycled electrode.

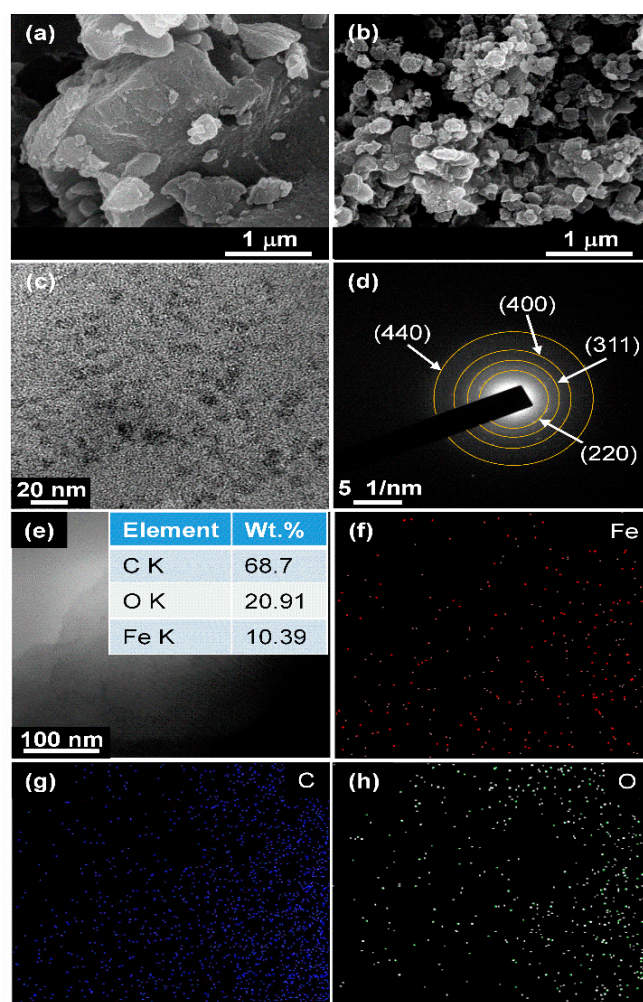


Figure 11. SEM images of (a) uncycled and (b) cycled $\text{Fe}_3\text{O}_4(13)@C9$ anode. (c) TEM image of cycled electrode; (d) SAED pattern and (e–h) EDX elemental mapping of cycled $\text{Fe}_3\text{O}_4(13)@C9$ anode.

The splitting of a few particles to a smaller size and then aggregation of these particles was observed for the cycled anode. The TEM image in Figure 11c exhibited well-distributed Fe_3O_4 nanoparticles confined in CMK-9 scaffolds. The SAED pattern in Figure 11d exhibited diffraction rings for the planes (220), (311), (400) and (440) of Fe_3O_4 nanoparticles, suggesting retention of the crystalline structure despite undergoing long-term charging and discharging cycles. The EDX elemental mapping in Figure 11e–h confirmed the presence

and uniform distribution of Fe, C and O in the Fe₃O₄(13)@C9 anode after 100 cycles. The results indicated that the electrode upheld almost similar morphological, microstructural and structural integrity even after prolonged charge–discharge cycles, demonstrating the excellent electrochemical performance of the Fe₃O₄(13)@C9 anode.

4. Conclusions

In summary, Fe₃O₄ nanoparticles embedded in 3D bimodal porous carbon CMK-9 nanocomposites were synthesized by following nanocasting and wet-impregnation strategies, and their electrochemical performances as anodes for LIBs were assessed systematically. The impregnation of Fe₃O₄ NPs into the mesopores of CMK-9 enhanced the electrochemical responses of the Fe₃O₄(*x*)@C9 nanocomposites. Among the nanocomposites investigated, the Fe₃O₄(13)@C9 nanocomposite exhibited an excellent discharge capacity of 1222 mA h g^{−1} after 150 cycles at a current rate of 100 mA g^{−1} with a retention capacity of 96.8% compared to the 4th cycle. At a higher current rate of 1000 mA g^{−1}, the Fe₃O₄(13)@C9 electrode delivered a discharge capacity of 636 mA h g^{−1} after 300 cycles and retained a capacity of 85% in comparison to the 4th cycle capacity. The excellent electrochemical performances of the Fe₃O₄(13)@C9 anode were attributed to a combination of a number of factors, namely the 3D interlinked mesoporous scaffold of CMK-9 that acted as extra Li⁺-ion storage sites and the confinement of Fe₃O₄ NPs inside the mesopores prevented aggregation which mitigated volume expansion and could retain electrolytes within the mesopores of CMK-9 resulting improved electrode/electrolyte interactions, higher lithium diffusion coefficient and synergistic effects between Fe₃O₄ NPs and CMK-9 in terms of structure and lithium-ion storage. The excellent capacity, superior rate capability and steady and long cycle life of the Fe₃O₄(13)@C9 nanocomposite revealed its promising potential as an anode for LIBs.

Supplementary Materials: The following supporting information can be downloaded at <https://www.mdpi.com/article/10.3390/batteries9100482/s1>. Figure S1: Cycle performance of pristine Fe₃O₄ nanoparticles at a current density of 1000 mA g^{−1}; Figure S2: EIS spectra of (a) pristine CMK-9, (b) Fe₃O₄(4)@C9, (c) Fe₃O₄(8)@C9, (d) Fe₃O₄(13)@C9, (e) Fe₃O₄(18)@C9 and (f) Fe₃O₄(25)@C9 anodes after 100 cycles; Figure S3: Z' vs. ω^{−1/2} plots of (a) pristine CMK-9, (b) Fe₃O₄(4)@C9, (c) Fe₃O₄(8)@C9, (d) Fe₃O₄(13)@C9, (e) Fe₃O₄(18)@C9 and (f) Fe₃O₄(25)@C9 anodes; Table S1: Comparison of electrochemical performance of Fe₃O₄(13)@C9 with other similar anode materials reported for lithium-ion batteries.

Author Contributions: Conceptualization, J.R.D., D.S. and H.-M.K.; methodology, J.R.D. and Y.-H.L.; validation, D.S. and Y.-H.L.; formal analysis, J.R.D. and D.S.; investigation, Y.-H.L. and D.S.; resources, H.-M.K.; data curation, Y.-H.L.; writing—original draft preparation, J.R.D. and D.S.; writing—review and editing, H.-M.K. and Y.-C.Y.; visualization, J.R.D. and Y.-H.L.; supervision, H.-M.K.; project administration, H.-M.K. and Y.-C.Y.; funding acquisition, H.-M.K. and Y.-C.Y. All authors have read and agreed to the published version of the manuscript.

Funding: This research was funded by the National Science and Technology Council of Taiwan (Grant number: MOST 110-2113-M-008-MY3), the NCU-Covestro Research Center and the National Taipei University of Technology, Taiwan.

Institutional Review Board Statement: Not applicable.

Informed Consent Statement: Not applicable.

Data Availability Statement: The data presented in this study are available on request.

Acknowledgments: The authors acknowledge the NCU valuable instrument center for XPS, FESEM, TEM and TGA measurements.

Conflicts of Interest: The authors declare no conflict of interest.

References

1. Link, S.; Neef, C.; Wicke, T. Trends in automotive battery cell design: A statistical analysis of empirical data. *Batteries* **2023**, *9*, 261. [[CrossRef](#)]
2. Choi, D.; Shamim, N.; Crawford, A.; Huang, Q.; Vartanian, C.K.; Viswanathan, V.V.; Paiss, M.D.; Alam, M.J.; Reed, D.M.; Sprenkle, V.L. Li-ion battery technology for grid application. *J. Power Sources* **2021**, *511*, 230419. [[CrossRef](#)]
3. He, L.; Xu, C.; Ma, P.; Wang, Q. Synthesis and characterization of Mn₂O₃ nanorods as anode materials for lithium ion batteries. *Int. J. Electrochem. Sci.* **2020**, *15*, 5908–5915. [[CrossRef](#)]
4. Zhang, L.; Song, J.; Liu, Y.; Yuan, X.; Guo, S. Tailoring nanostructured MnO₂ as anodes for lithium ion batteries with high reversible capacity and initial coulombic efficiency. *J. Power Sources* **2018**, *379*, 68–73. [[CrossRef](#)]
5. Dai, L.; Zhong, X.; Zou, J.; Fu, B.; Su, Y.; Ren, C.; Wang, J.; Zhong, G. Highly ordered SnO₂ nanopillar array as binder-free anodes for long-life and high-rate Li-ion batteries. *Nanomaterials* **2021**, *11*, 1307. [[CrossRef](#)]
6. Chang, J.H.; Cheong, J.Y.; Shim, Y.; Park, J.Y.; Kim, S.J.; Lee, J.; Lee, H.J.; Lim, H.; Liu, W.; Zhang, Q.; et al. Unravelling high volumetric capacity of Co₃O₄ nanograin-interconnected secondary particles for lithium-ion battery anodes. *J. Mater. Chem. A* **2021**, *9*, 6242–6251. [[CrossRef](#)]
7. Chang, L.; Wang, K.; Huang, L.; He, Z.; Shao, H.; Wang, J. Hierarchically porous CoO microsphere films with enhanced lithium/sodium storage properties. *J. Alloys Compd.* **2017**, *725*, 824–834. [[CrossRef](#)]
8. Hwang, J.; Yadav, D.; Yang, H.; Jeon, I.; Yang, D.; Seo, J.-W.; Kang, M.; Jeong, S.-Y.; Cho, C.-R. In situ electrochemical impedance measurements of α -Fe₂O₃ nanofibers: Unravelling the Li-ion conduction mechanism in Li-ion batteries. *Batteries* **2022**, *8*, 44. [[CrossRef](#)]
9. Maroni, F.; Gabrielli, S.; Palmieri, A.; Marcantoni, E.; Croce, F.; Nobili, F. High cycling stability of anodes for lithium-ion batteries based on Fe₃O₄ nanoparticles and poly(acrylic acid) binder. *J. Power Sources* **2016**, *332*, 79–87. [[CrossRef](#)]
10. Chen, X.; Zhu, X.; Cao, G.; Zhang, S.; Mu, Y.; Ming, H.; Qiu, J. Fe₃O₄-based anodes with high conductivity and fast ion diffusivity designed for high-energy lithium-ion batteries. *Energy Fuels* **2021**, *35*, 1810–1819. [[CrossRef](#)]
11. Yang, C.; Wang, X.; Ren, Y.; Gu, S.; Wang, Q.; Li, H.; Yue, K.; Gao, T.; Zhou, G. NiFe₂V₂O₈@N-doped carbon yolk-double shell spheres for efficient lithium storage. *Chem. Eng. J.* **2023**, *454*, 140045. [[CrossRef](#)]
12. Ren, Y.; Li, X.; Wang, Y.; Gong, Q.; Gu, S.; Gao, T.; Sun, X.; Zhou, G. Self-template formation of porous yolk-shell structure Mo-doped NiCo₂O₄ toward enhanced lithium storage performance as anode material. *J. Mater. Sci. Technol.* **2022**, *102*, 186–194. [[CrossRef](#)]
13. Maroni, F.; Bruni, P.; Suzuki, N.; Aihara, Y.; Gabrielli, S.; Carbonari, G.; Agostini, M.; Branchi, M.; Ferrari, S.; Navarra, M.A.; et al. Highly stable Fe₃O₄/C composite: A candidate material for all solid-state lithium-ion batteries. *J. Electrochem. Soc.* **2020**, *167*, 070556. [[CrossRef](#)]
14. Rehman, W.; Jiang, Z.; Qu, Z.; Wang, X.; Du, X.; Ghani, A.; Kabir, F.; Xu, Y. Porous carbon derived from cherry blossom leaves treatment with Fe₃O₄ enhanced the electrochemical performance of a lithium storage anode. *Electrochim. Acta* **2023**, *455*, 142426. [[CrossRef](#)]
15. Xia, Z.Y.; Wei, D.; Anitowska, E.; Bellani, V.; Ortolani, L.; Morandi, V.; Gazzano, M.; Zanelli, A.; Borini, S.; Palermo, V. Electrochemically exfoliated graphene oxide/iron oxide composite foams for lithium storage, produced by simultaneous graphene reduction and Fe(OH)₃ condensation. *Carbon* **2015**, *84*, 254–262. [[CrossRef](#)]
16. Saikia, D.; Deka, J.R.; Lin, C.-W.; Lai, Y.-H.; Zeng, Y.-H.; Chen, P.-H.; Kao, H.-M.; Yang, Y.-C. Insight into the superior lithium storage properties of ultrafine CoO nanoparticles confined in a 3D bimodal ordered mesoporous carbon CMK-9 anode. *ChemSusChem* **2020**, *13*, 2952–2965. [[CrossRef](#)]
17. Ban, C.; Wu, Z.; Gillaspie, D.T.; Chen, L.; Yan, Y.; Blackburn, J.L.; Dillon, A.C. Nanostructured Fe₃O₄/SWNT electrode: Binder-free and high-rate Li-ion anode. *Adv. Mater.* **2010**, *22*, E145–E149. [[CrossRef](#)]
18. Velásquez, C.A.; Vásquez, F.A.; Alvarez-Láinez, M.; Zapata-González, A.; Calderón, J.A. Carbon nanofibers impregnated with Fe₃O₄ nanoparticles as a flexible and high capacity negative electrode for lithium-ion batteries. *J. Alloys Compd.* **2021**, *862*, 158045. [[CrossRef](#)]
19. Li, H.; Wang, J.; Li, Y.; Zhao, Y.; Tian, Y.; Kurmanbayeva, I.; Bakenov, Z. Hierarchical sandwiched Fe₃O₄@C/graphene composite as anode material for lithium-ion batteries. *J. Electroanal. Chem.* **2019**, *847*, 113240. [[CrossRef](#)]
20. Zhao, P.; Jiang, L.; Li, P.; Xiong, B.; Zhou, N.; Liu, C.; Jia, J.; Ma, G.; Zhang, M. Tailored engineering of Fe₃O₄ and reduced graphene oxide coupled architecture to realize the full potential as electrode materials for lithium-ion batteries. *J. Colloid Interface Sci.* **2023**, *634*, 737–746. [[CrossRef](#)]
21. Yan, Y.; Lu, X.; Li, Y.; Song, J.; Tian, Q.; Yang, L.; Sui, Z. Dispersive Fe₃O₄ encapsulated in porous carbon for high capacity and long life anode of lithium-ion batteries. *J. Alloys Compd.* **2022**, *899*, 163342. [[CrossRef](#)]
22. Hwang, J.-K.; Lim, H.-S.; Sun, Y.-K.; Suh, K.-D. Monodispersed hollow carbon/Fe₃O₄ composite microspheres for high performance anode materials in lithium-ion batteries. *J. Power Sources* **2013**, *244*, 538–543. [[CrossRef](#)]
23. Jia, P.; Sun, J.; Jiang, Z.; Wang, W.; Song, Z.; Mao, Y.; Zhao, X. Construction of N-doped porous carbon-coated Fe₃O₄ with efficient ion transfer performance for enhanced-performance lithium storage. *Electrochim. Acta* **2022**, *428*, 140935. [[CrossRef](#)]
24. Inagaki, M.; Toyoda, M.; Soneda, Y.; Tsujimura, S.; Morishita, T. Templated mesoporous carbons: Synthesis and applications. *Carbon* **2016**, *107*, 448–473. [[CrossRef](#)]

25. Eftekhari, A.; Fan, Z. Ordered mesoporous carbon and its applications for electrochemical energy storage and conversion. *Mater. Chem. Front.* **2017**, *1*, 1001–1027. [[CrossRef](#)]
26. Meng, Y.; Gu, D.; Zhang, F.Q.; Shi, Y.F.; Yang, H.F.; Li, Z.; Yu, C.Z.; Tu, B.; Zhao, D.Y. Ordered mesoporous polymers and homologous carbon frameworks: Amphiphilic surfactant templating and direct transformation. *Angew. Chem. Int. Ed.* **2005**, *44*, 7053–7059. [[CrossRef](#)]
27. Meng, Y.; Gu, D.; Zhang, F.Q.; Shi, Y.F.; Cheng, L.; Feng, D.; Wu, Z.X.; Chen, Z.X.; Wan, Y.; Stein, A.; et al. A family of highly ordered mesoporous polymer resin and carbon structures from organic-organic self-assembly. *Chem. Mater.* **2006**, *18*, 4447–4464. [[CrossRef](#)]
28. Jun, S.; Joo, S.H.; Ryoo, R.; Kruk, M.; Jaroniec, M.; Liu, Z.; Ohsuna, T.; Terasaki, O. Synthesis of new, nanoporous carbon with hexagonally ordered mesostructure. *J. Am. Chem. Soc.* **2000**, *122*, 10712–10713. [[CrossRef](#)]
29. Ryoo, R.; Joo, S.H.; Kruk, M.; Jaroniec, M. Ordered mesoporous carbons. *Adv. Mater.* **2001**, *13*, 677–681. [[CrossRef](#)]
30. Lu, A.-H.; Schüth, F. Nanocasting: A versatile strategy for creating nanostructured porous materials. *Adv. Mater.* **2006**, *18*, 1793–1805. [[CrossRef](#)]
31. Kleitz, F.; Choi, S.H.; Ryoo, R. Cubic *Ia3d* large mesoporous silica: Synthesis and replication to platinum nanowires, carbon nanorods and carbon nanotubes. *Chem. Commun.* **2003**, 2136–2137. [[CrossRef](#)] [[PubMed](#)]
32. Wang, X.; Liang, C.; Dai, S. Nano/microporous materials: Mesoporous and surface-functionalized mesoporous carbon. In *Encyclopedia of Inorganic and Bioinorganic Chemistry*; John Wiley & Sons, Ltd.: Hoboken, NJ, USA, 2009; pp. 1–18. [[CrossRef](#)]
33. Wu, F.; Huang, R.; Mu, D.; Shen, X.; Wu, B. A novel composite with highly dispersed Fe₃O₄ nanocrystals on ordered mesoporous carbon as an anode for lithium ion batteries. *J. Alloys Compd.* **2014**, *585*, 783–789. [[CrossRef](#)]
34. Cao, Z.; Ma, X. Encapsulated Fe₃O₄ into tubular mesoporous carbon as a superior performance anode material for lithium-ion batteries. *J. Alloys Compd.* **2020**, *815*, 152542. [[CrossRef](#)]
35. Zhang, H.; Tao, H.; Jiang, Y.; Jiao, Z.; Wu, M.; Zhao, B. Ordered CoO/CMK-3 nanocomposites as the anode materials for lithium-ion batteries. *J. Power Sources* **2010**, *195*, 2950–2955. [[CrossRef](#)]
36. Panja, T.; Bhattacharjya, D.; Yu, J.-S. Nitrogen and phosphorus co-doped cubic ordered mesoporous carbon as a supercapacitor electrode material with extraordinary cyclic stability. *J. Mater. Chem. A* **2015**, *3*, 18001–18009. [[CrossRef](#)]
37. Zhang, P.; Qiu, J.; Zheng, Z.; Liu, G.; Ling, M.; Martens, W. Free-standing and bendable carbon nanotubes/TiO₂ nanofibres composite electrodes for flexible lithium ion batteries. *Electrochim. Acta* **2013**, *104*, 41–47. [[CrossRef](#)]
38. Mao, J.Y.; Niu, D.C.; Zheng, N.; Jiang, G.Y.; Zhao, W.R.; Shi, J.L.; Li, Y.S. Fe₃O₄-embedded and N-doped hierarchically porous carbon nanospheres as high-performance lithium ion battery anodes. *ACS Sustain. Chem. Eng.* **2019**, *7*, 3424–3433. [[CrossRef](#)]
39. Chen, Y.; Song, B.; Li, M.; Lu, L.; Xue, J. Fe₃O₄ nanoparticles embedded in uniform mesoporous carbon spheres for superior high-rate battery applications. *Adv. Funct. Mater.* **2014**, *24*, 319–326. [[CrossRef](#)]
40. Cui, Y.P.; Feng, W.T.; Liu, W.; Li, J.J.; Zhang, Y.; Du, Y.X.; Li, M.Z.; Huang, W.; Wang, H.L.; Liu, S. Template-assisted loading of Fe₃O₄ nanoparticles inside hollow carbon “rooms” to achieve high volumetric lithium storage. *Nanoscale* **2020**, *12*, 10816–10826. [[CrossRef](#)]
41. Kopuklu, B.B.; Tasdemir, A.; Gursel, S.A.; Yurum, A. High stability graphene oxide aerogel supported ultrafine Fe₃O₄ particles with superior performance as a Li-ion battery anode. *Carbon* **2021**, *174*, 158–172. [[CrossRef](#)]
42. Liu, Y.; He, D.; Tan, Q.; Wan, Q.; Han, K.; Liu, Z.; Li, P.; An, F.; Qu, X. A synergetic strategy for an advanced electrode with Fe₃O₄ embedded in a 3D N-doped porous graphene framework and a strong adhesive binder for lithium/potassium ion batteries with an ultralong cycle lifespan. *J. Mater. Chem. A* **2019**, *7*, 19430–19441. [[CrossRef](#)]
43. Saikia, D.; Deka, J.R.; Lu, B.-J.; Chen, Y.-C.; Lian, J.-W.; Kao, H.-M.; Yang, Y.-C. Pinecone-derived biomass carbons as anodes for lithium and sodium-ion batteries by template-assisted and chemically activated approaches. *J. Power Sources* **2023**, *580*, 233329. [[CrossRef](#)]
44. Tu, M.; Yang, C.; Zhang, R.; Kong, X.; Jia, R.; Yu, L.; Xu, B. One-step engineering carbon supported magnetite nanoparticles composite in a submicron pomegranate configuration for superior lithium-ion storage. *Materials* **2023**, *16*, 313. [[CrossRef](#)] [[PubMed](#)]
45. Saikia, D.; Deka, J.R.; Zeng, Y.-H.; Hsu, H.-C.; Chen, Y.-C.; Kao, H.-M.; Yang, Y.-C. New insights into the outstanding performances of nickel doped manganese oxide nanoparticles embedded in a 3D carbon nanopipes framework as anode for lithium and sodium-ion batteries. *Int. J. Energy Res.* **2022**, *46*, 22454–22473. [[CrossRef](#)]
46. Fromm, O.; Heckmann, A.; Rodehorst, U.C.; Frerichs, J.; Becker, D.; Winter, M.; Placke, T. Carbons from biomass precursors as anode materials for lithium ion batteries: New insights into carbonization and graphitization behavior and into their correlation to electrochemical performance. *Carbon* **2018**, *128*, 147–163. [[CrossRef](#)]
47. Chen, S.; Wu, Q.; Wen, M.; Wu, Q.; Li, J.; Cui, Y.; Pinna, N.; Fan, Y.; Wu, T. Sea-sponge like structure of nano-Fe₃O₄ on skeleton-C with long cycle life under high rate for li-ion batteries. *ACS Appl. Mater. Interfaces* **2018**, *10*, 19656–19663. [[CrossRef](#)] [[PubMed](#)]
48. Fang, B.; Kim, M.-S.; Kim, J.H.; Lim, S.; Yu, J.-S. Ordered multimodal porous carbon with hierarchical nanostructure for high Li storage capacity and good cycling performance. *J. Mater. Chem.* **2010**, *20*, 10253–10259. [[CrossRef](#)]
49. Saikia, D.; Wang, T.-H.; Chou, C.-J.; Fang, J.; Tsai, L.-D.; Kao, H.-M. A comparative study of ordered mesoporous carbons with different pore structures as anode materials for lithium-ion batteries. *RSC Adv.* **2015**, *5*, 42922–42930. [[CrossRef](#)]
50. Yang, Y.; Li, J.; Chen, D.; Zhao, J. A facile electrophoretic deposition route to the Fe₃O₄/CNTs/rGO composite electrode as a binder-free anode for lithium ion battery. *ACS Appl. Mater. Interfaces* **2016**, *8*, 26730–26739. [[CrossRef](#)]

51. Zhang, Y.; Zhang, Y.; Zhang, K.; Jia, K.; Liu, G.; He, X.; Liu, W.; Li, K.; Zhang, Z. Nitrogen-doped graphene nanosheet coated nanospherical Fe₃O₄ from zeolitic imidazolate frameworks template as anode of lithium ion batteries. *Energy Fuels* **2020**, *34*, 14986–14994. [[CrossRef](#)]
52. Zhao, J.; Yang, B.; Zheng, Z.; Yang, J.; Yang, Z.; Zhang, P.; Ren, W.; Yan, X. Facile preparation of one-dimensional wrapping structure: Graphene nanoscroll-wrapped of Fe₃O₄ nanoparticles and its application for lithium-ion battery. *ACS Appl. Mater. Interfaces* **2014**, *6*, 9890–9896. [[CrossRef](#)] [[PubMed](#)]
53. Zhao, X.; Xia, D.; Zheng, K. Fe₃O₄/Fe/Carbon composite and its application as anode material for lithium-ion batteries. *ACS Appl. Mater. Interfaces* **2012**, *4*, 1350–1356. [[CrossRef](#)] [[PubMed](#)]
54. He, Z.; Wang, K.; Zhu, S.; Huang, L.; Chen, M.; Guo, J.; Pei, S.; Shao, H.; Wang, J. MOF-derived hierarchical MnO-doped Fe₃O₄@C composite nanospheres with enhanced lithium storage. *ACS Appl. Mater. Interfaces* **2018**, *10*, 10974–10985. [[CrossRef](#)] [[PubMed](#)]
55. Li, D.; Li, X.; Wang, S.; Zheng, Y.; Qiao, L.; He, D. Carbon-wrapped Fe₃O₄ nanoparticle films grown on nickel foam as binder-free anodes for high-rate and long-life lithium storage. *ACS Appl. Mater. Interfaces* **2014**, *6*, 648–654. [[CrossRef](#)]
56. Staffolani, A.; Darjazi, H.; Carbonari, G.; Maroni, F.; Gabrielli, S.; Nobili, F. Fe₃O₄/graphene composite anode material for fast-charging Li-ion batteries. *Molecules* **2021**, *26*, 4316. [[CrossRef](#)] [[PubMed](#)]
57. Chen, M.; Shen, X.; Chen, K.; Wu, Q.; Zhang, P.; Zhang, X.; Diao, G. Nitrogen-doped mesoporous carbon-encapsulation urchin-like Fe₃O₄ as anode materials for high performance Li-ions batteries. *Electrochim. Acta* **2016**, *195*, 94–105. [[CrossRef](#)]
58. Srinivasan, N.R.; Mitra, S.; Bandyopadhyaya, R. Improved electrochemical performance of SnO₂-mesoporous carbon hybrid as a negative electrode for lithium ion battery applications. *Phys. Chem. Chem. Phys.* **2014**, *16*, 6630–6640. [[CrossRef](#)]
59. Gao, C.W.; Jiang, Z.J.; Wang, P.X.; Jensen, L.R.; Zhang, Y.F.; Yue, Y.Z. Optimized assembling of MOF/SnO₂/Graphene leads to superior anode for lithium ion batteries. *Nano Energy* **2020**, *74*, 104868. [[CrossRef](#)]

Disclaimer/Publisher's Note: The statements, opinions and data contained in all publications are solely those of the individual author(s) and contributor(s) and not of MDPI and/or the editor(s). MDPI and/or the editor(s) disclaim responsibility for any injury to people or property resulting from any ideas, methods, instructions or products referred to in the content.